Metabolomics assisted with stable-isotope labeling: exploring neuronal metabolism related to Parkinson's disease

Huang, L.

Chapter 3:

Unraveling the metabolic dysfunction processes fueling parkinsonism pathogenesis in human iPSC-derived mid-brain neurons with PINK1 mutation and rotenone exposure

Based on:

Luojiao Huang, Vincent Verschoor, Agnieszka Wegrzyn, Fadhilah Rachmi Rosmasari, Wei Yang, Alida Kindt-Dunjko, Jens C. Schwamborn, Christine Klein, Amy Harms, Ronan Fleming, Thomas Hankemeier

Unraveling the Metabolic Dysfunction Processes Fueling Parkinsonism Pathogenesis in Human iPSC-derived Mid-brain Neurons with PINK1 Mutation and Rotenone Exposure

Manuscript submitted

Abstract

Parkinson's disease (PD) is a complex neurodegenerative disease and can be triggered by multiple risk factors, such as genetic alterations, environmental or occupational exposures, and aging. It is characterized by the loss of dopaminergic neurons. However, until now, no clear molecular mechanism driving neuronal death has been well understood and no intrinsically effective therapy is available. In this study, we used human induced pluripotent stem cell (iPSC)-derived mid-brain neuronal models to investigate the separate and combined effects of a phosphatase and tensin homolog-induced kinase 1 (PINK1) mutation and rotenone exposure by comparative metabolomics of central carbon metabolism, acylcarnitine and polyunsaturated fatty acid metabolism. Neurons with PINK1 mutation or rotenone exposure both revealed varying extents of metabolic disturbances in terms of energy imbalance, mitochondrial respiratory impairment, oxidative stress and neuronal inflammation. Moreover, rotenone negatively impacted antioxidant capacity. These overlapping and compensating disturbances ultimately led to a broad metabolic dysregulation in the mutation model and toxicant exposure. In addition, β-nicotinamide adenine dinucleotide (NAD+) supplementation to the rotenone-treated PINK1-mutant neurons improved the branched chain amino acid metabolism, resulting in increased energy production. These results suggest that gene-environmental interactions contribute to the complexity of neurodegeneration from a metabolic perspective. NAD+ supplementation for the in vitro cellular PD model shows its limitations in ameliorating these disturbances. Overall, our study provides valuable insights into a deeper understanding of parkinsonism pathogenesis.

Introduction

Parkinson's disease (PD), a prevalent neurodegenerative disease in the aging population, is characterized by severe motor symptoms and developing mental health problems [1]. As the worldwide aging population grows and life expectancy increases, the continuously increased prevalence and incidence of PD can pose a big challenge to global health and economics [2]. PD is a complex and multifactorial disease, with genetic alterations, environmental or occupational exposures and aging all playing a role [2,3].

Mutations in phosphatase and tensin homolog-induced kinase 1 (PINK1) have been typically identified in familial early-onset PD cases [4], causing a failure of cellular mitophagy to remove damaged mitochondria. Patients with this monogenic form of PD were reported to have symptoms clinically identical to those of patients with sporadic forms of PD [5,6]. PINK1 deficiency is associated with mitochondrial dysfunction, which is regarded as a hallmark of PD. Elucidating the relevant molecular mechanisms could also help to identify the key mechanism underlying the more prevalent sporadic PD [7]. Besides, PINK1 deficiency was reported incapable to induce neuronal loss, which makes scientists reconsider its role during neurodegeneration [8,9]. On the other hand, environmental toxins have been identified that increase the risk of developing PD, such as pesticides paraquat or rotenone [10]. Rotenone is a classic mitochondrial complex I inhibitor, inducing acute parkinsonian syndrome [11]. Since mitochondrial defects are commonly found in genetic and toxin perturbations, the role of genome-environment interactions becomes highly interesting and generates a possible hypothesis that genetic deficiency involved in mitochondrial-stress pathways could increase the susceptibility towards neurodegeneration in response to environmental toxins [12,13]. Expanding the investigation of the mechanisms from mono-cause to dual-cause intervention can gain more insights into the pathogenesis of sporadic PD.

Complex interactions between genotype, lifestyle, environmental exposure, and drug treatment result in diverse metabolic phenotypes in individuals, which fortunately can be identified and quantified at the level of endogenous metabolites or exogenous small molecules/metabolites [14]. Metabolomic technologies provide unique advantages in systematic measurements of metabolic pathway alterations associated with diseased conditions [15]. In order to probe into the PD pathogenesis mechanism, previous metabolomics studies majorly focused on measuring brain tissues from toxin-induced PD animal models (mouse, rat, goldfish, drosophila) and have revealed abnormal metabolic activities in glycolysis, tricarboxylic acid cycle (TCA), amino acids metabolism, nucleotides synthesis, fatty acids and lipids metabolism [16–21]. Few transgenic animal models have been generated that are implemented for PD metabolomics investigation other

than the alpha-synuclein transgenic mouse model [22,23]. A significant increase of guanosine level was discovered in the aged PD-related alpha-synuclein A53T transgenic mice, indicating a protective mechanism against neurodegeneration [23]. In-vitro cellular models, especially the induced pluripotent stem cell (iPSC)-derived model, give more flexibility in studying metabolomic perturbations caused by selective toxins or inhibitors [24,25], or patient-specific gene deficiency [26]. However, limited metabolomics studies at the cellular level have been carried out, and to our knowledge, there has been no report showing the metabolomic profile of human iPSC-derived neurons with PINK1 deficiency, let alone the interaction with toxin perturbations.

Mitochondria act as a major energy source for maintaining cellular functions and are highly abundant in neurons to support their high-rate energy consumption. Dysfunctional mitochondria are closely linked to disturbed metabolic energy homeostasis and play an important role in neurodegeneration [27]. β-nicotinamide adenine dinucleotide (NAD+) is an essential cofactor in cellular energy metabolism and is also a critical signaling pathway regulator in cell survival and neuroprotection [28]. NAD+ depletion has been widely reported in many PD-related animal and cellular models [29]. Current PD treatments are primarily dopamine-based and symptomatic in order to improve motor outcomes. No pharmacologic treatments for slowing or ameliorating neuronal degeneration are available. The supplementation of NAD+ or its precursors has the potential to become a promising therapeutic strategy [30,31].

In this study, we aimed first to identify metabolic dysregulations in the metabolome of dopaminergic neurons, aroused by PINK1 mutation, rotenone toxicity, and their interactive effects, and second, to assess the efficacy of NAD+ supplementation as a treatment for reversing the aforementioned disturbed metabolic phenotypes. We performed targeted metabolic profiling on the iPSC-derived mid-brain neuron models cultured from a PINK1-mutant and its gene-corrected cell line and evaluated changes brought on by rotenone treatment. Our results revealed systemic metabolic pathway alterations from glucose, amino acid, nucleotide, acylcarnitine, and fatty acid metabolism related to neuronal energy failure and oxidative stress. Moreover, for the first time, we showed how impaired mitochondrial homeostasis in PINK1-mutant neurons responded to rotenone perturbation, which contributes to a deeper understanding of potential PD pathogenesis mechanisms. In terms of the identified disturbed metabolism, we further demonstrated the limited ability of NAD+ treatment in energy restoration for PINK1 parkinsonism, which provides valuable hints for improving future potential therapies in ameliorating neuronal degeneration.

Materials and methods

1. In vitro cell culture

Information on isogenic pairs of wild-type and mutant human neuroepithelial stem cell (hNESC) lines from an early-onset PD patient with a PINK1-Q456X mutation can be found in details in Table S1. The PINK1-mutant and its isogenic control hNESCs (cell line ID: M826 and GC826) were maintained and generated into midbrain-specific dopaminergic neurons by following an established protocol [32,33], with some adaptions mentioned in the sections below. The same adaptions were also applied in our previous work [34].

1.1 N2B27 medium preparation

The culture medium, denoted N2B27 medium, was used as the basis to prepare both maintenance and differentiation media. N2B27 was prepared by mixing 24 mL Neurobasal medium (Life Technologies, USA), 24 mL of Dulbecco's Modified Eagle Medium: Nutrient Mixture F-12 (DMEM/F12) medium (Life Technologies, USA) supplemented with 1% penicillin and streptomycin (Life Technologies, USA), 0.5 mL of 200 mM L-glutamine (Life Technologies, USA), 0.5 mL of B27 supplement without Vitamin A and 0.25 mL of N2 supplement (Life Technologies, USA) to reach a total volume of 49.25 mL.

1.2 Plate coating and culture group design

New cell-culture treated 6/12-well plates (ThermoFisher scientific, USA) were coated with 1% Matrigel (Corning, USA, Catalogue number: Cat #354277) in 1000/600 μL of DMEM (1X) medium supplemented with knockout serum replacement (ThermoFisher scientific, USA). Four wells from 6-well plate were used for propagation of each cell line. Each cell line was next cultured on 12-well plates in five conditions including control, dimethyl sulfoxide (DMSO) control, rotenone treatment, NAD+ treatment, and combined treatment.

1.3 Cell seeding and maintenance

The medium to maintain the hNESC in culture, denoted maintenance medium, was based on N2B27 medium with 0.5 μM purmorphamine (PMA, Enzo life sciences, USA), 3 μM CHIR-99021 (Axon Medchem, The Netherlands) and 150 μM ascorbic acid (Sigma Aldrich, USA). Each cell line was propagated on 6-well plates till reaching 80-90% confluency and enzymatically passaged with Accutase (ThermoFisher scientific, USA) onto precoated 12-well plates. Recollected cells were seeded in six replicate wells per condition group on 12-well plates. The cell seeding on 12-well plate was done by preparing 4×10^5 million cells/mL in maintenance medium and adding 300 μL of this preparation together with another 300 μL of maintenance medium to reach 1.2×10^5 cells per well. The plate was incubated at 37 °C and 5% CO_2 for 48 h.

1.4 Neuronal differentiation and maturation

The differentiation medium with PMA preparation to induce the differentiation of hNESC towards midbrain dopaminergic neurons consisted of N2B27 medium with 200 μM ascorbic acid, 0.01 ng/ μL brain-derived neurotropic factor (BDNF, Peprotech, USA), 0.01 ng/μL

glial cell line-derived neurotrophic factor (GDNF, Peprotech, USA), 0.001 ng/µL transforming growth factor beta-3 (TGFβ-3, Peprotech, USA), 2.5 µM dibutyryl cyclic adenosine monophosphate (dbcAMP) (Sigma Aldrich, USA) and 1 µM PMA. This medium preparation was completely replaced every 2 days during the next 6 days of culture in the differentiation process. For the maturation of differentiated neurons, PMA is required to be absent from the differentiation medium. This differentiation medium without PMA was used from day 9 onwards and complete media replacement was done every 2 days for 2 weeks.

1.5 Neuron treatment with rotenone or NAD+

After 21 days of neuron differentiation and maturation, neurons in the rotenone group were exposed to 400 nM rotenone (dissolved by DMSO) for 24 hours, and neurons in the NAD+ group were supplemented with 2 mM NAD+ for 24 hours. Neurons in the combined treatment group were first treated with 400 nM rotenone for 24 hours. After that, neurons were cultured for another 24 hours with medium containing 2 mM NAD+ to replace the used rotenone medium. In the control group, the cells were given differentiation medium containing no additional compound. In the DMSO control group, the cells were given differentiation medium with the same amount of DMSO as in the rotenone treatment.

1.6 Cell and medium sample harvest

The spent medium was collected into a 1.5 mL Eppendorf tube. For cell quenching, 200 uL of ice-cold 80% MeOH in water was used immediately after removing the spent medium and washing with phosphate buffered saline (PBS, Gibco/Life Technologies, USA). Quenched cell lysate was harvested into a new Eppendorf tube. All sample tubes were fast frozen into liquid nitrogen and stored in the -80 °C freezer until LC-MS measurement.

2. Sample preparation and LC-MS measurement

Cell samples were lysed with sonication after one freeze-thaw cycle, vortexed and then centrifuged at 16000 g 4 ℃ for 10 min. Cell pellets were collected for measuring the total protein content later. Supernatants were transferred into clean 1.5 mL Eppendorf tubes and evaporated to dryness in a Labcono SpeedVac (MO, United State). Each sample was reconstituted with 75 µL ice cold methanol/water (80%/20%; v/v). 50 µL of the sample reconstitution volume was collected and transferred into a new Eppendorf tube for polar metabolome measurement. Next, 10 µL of the sample reconstitution volume was collected and transferred into a new Eppendorf tube for acylcarnitine measurement. The remaining volume per sample was pooled together as a quality control (QC) sample pool. In total, 10 QC samples with 50 uL were prepared for polar metabolome measurement, and 10 QC samples with 10 uL were prepared for acylcarnitine metabolome measurement.

Polar metabolome: Cell lysate samples aliquoted for polar metabolome measurement followed a liquid-liquid extraction (LLE) method that was described in our previous work. 5 uL of polar ISTD solution was added into each sample, which was then followed with LLE extraction by an ice-cold solvent mixed with methanol/water/chloroform. The final upper phase was transferred into a new Eppendorf tube and taken to dryness. The residue was reconstituted with 50 µL of ice-cold methanol/water (1:1 v/v). Finally, 45 µL of reconstitution solution was transferred into an autosampler vial with glass insert for LC-MS measurement [35].

Acylcarnitines: Cell lysate samples aliquoted for acylcarnitine measurement were processed using a protein precipitation method. An ice-cold crash solvent was prepared by mixing 20% acylcarnitine ISTD solution with 80% methanol solvent. 30 uL of the crash solvent was added into each sample, which was then followed with vortexing for 10 mins, centrifuging at 16000 rcf, 4 ℃ for 10 min. Finally, 35 µL of the supernatant was transferred into an autosampler vial with glass insert for LC-MS measurement.

Signaling lipids: Medium samples aliquoted for signaling lipids measurement followed a liquid-liquid extraction (LLE) method with minor adaptions that was also described in our previous work [36]. Medium aliquots (100 uL) were thawed on ice, and then 10 µL antioxidant (0.2mg/ml butylated hydroxytoluene (BHT) and 0.2 mg/ml ethylenediaminetetraacetic acid (EDTA)) solution and 10 µL of signaling lipid ISTD solution were added. Samples were briefly vortexed and then acidified with 100 uL of buffer solution (0.2 M citric acid and 0.4 M disodium hydrogen phosphate buffer at pH 4.5). LLE was accomplished by adding 800 uL of a butanol (BuOH)/methyl tert-butyl ether (MTBE) (1:1 v/v) solution. Samples in Eppendorf tubes were settled on ice for 20 mins and transferred in the bullet blender to mix for 4 minutes at the speed of level 8. After a subsequent centrifugation at 16000 rcf, 4 ℃ for 10 min, 700 µL of the upper organic phase was collected and taken to dryness. The residue was reconstituted with 50 µL of ice-cold methanol/acetonitrile (7:3 v/v, with 100 nM CUDA). Finally, 45 µL of reconstitution solution was transferred into an autosampler vial with glass insert for LC-MS measurement.

3. LC-MS measurement

Polar metabolome: Targeted 106 polar metabolites analyses was performed on a SCIEX tripleTOF 5600 MS system (SCIEX, USA) coupled to a Waters Acquity UPLC Class II (Waters, USA) equipped with a SeQuant® ZIC®-cHILIC HPLC column (2.1mm x 100 mm, 3.0 µm, Merck, Germany). The LC-MS method followed a previously described method. Mobile phase A consisted of 90% acetonitrile, 10% water with 5 mM ammonium formate, and mobile phase B consisted of 10% acetonitrile, 90% water with 5 mM ammonium formate. The injection volume was 3 µL. The flow rate was 0.5 mL/min and the gradient

was as follows: 0 min-0% B, 2 min-15% B, 5 min-21% B, 7.5 min-26% B, from 10 to 11 min-40% B, from 11.5 to 18 min-0% B. Electrospray ionization (ESI) was operating at negative ion mode. The following ion source parameters were applied, spray voltage 4.5 kV, capillary temperature 400 °C, ion source gas 1 20 psi, ion source gas 2 50 psi, curtain gas 25 psi, CAD gas 7 psi [37].

Acylcarnitines: Targeted 50 acylcarnitine metabolites analyses was performed on a SCIEX QTRAP 6500 MS system (SCIEX, USA) coupled to a Waters Acquity UPLC Class II (Waters, USA) equipped with an AccQ-Tag™ Ultra C18 column (2.1mm x 100 mm, 1.7 µm, Waters, USA). In the LC-MS method, mobile phase A consisted of water with 0.1% formic acid, and mobile phase B consisted of acetonitrile with 0.1% formic acid. The injection volume was 5 µL. Separations were performed at 60 °C at a flow rate of 0.7 mL/min using the following gradient: from 0 to 1.10 min-5% B, from 1.11 to 2 min-11% B, 8 min-70% B, from 8.01 to 9.01 min-100% B, from 9.20 to 11 min-5% B. Electrospray ionization (ESI) was operating at positive ion mode, followed with a multiple reaction monitoring detection method. The applied ion source and compound parameters were shown below, spray voltage 4.5 kV, capillary temperature 350 °C, ion source gas 1 80 psi, ion source gas 1 70 psi, curtain gas 20 psi, CAD gas -2 psi, CXP 10 V, DP 70 V, EP 10 V [38].

Signaling lipids: Targeted 106 signaling lipid mediators were analyzed at low mobile phase pH condition. The analyses was performed on a SCIEX Triple Quad™ 7500 MS system (SCIEX, USA) coupled to a Shimadzu Nexera Prominence LC (Shimadzu, Japan) equipped with an Acquity BEH C18 column (50 × 2.1 mm, 1.7 µm; Waters, USA). In the LC-MS method, mobile phase A consisted of water with 0.1% acetic acid, mobile phase B consisted of a mixture of acetonitrile–methanol (9:1, v/v) with 0.1% acetic acid, mobile phase C consisted of isopropanol with 0.1% acetic acid. The injection volume was 5 µL. Separations were performed at 40 °C at a flow rate of 0.7 mL/min using the following gradient: 20% B and 1% C as starting conditions; changing to 85% B between 0.75 and 14 min and to 15% C between 11 and 14 min; conditions held for 0.5 min prior to column re-equilibration at the starting conditions from 14.8 to 16 min. Electrospray ionization (ESI) was operating at both positive and negative ion mode, followed with a multiple reaction monitoring detection method. The applied ion source parameters were, spray voltage 4.5 kV, capillary temperature 600 °C, ion source gas 1 65 psi, ion source gas 2 65 psi, curtain gas 45 psi, CAD gas 9 psi [36].

4. Immunofluorescence staining

At the end of differentiation stage, immunofluorescence staining was performed on the matured neurons of each cell line, GC826 and M826. Cells were fixed using 4%

formaldehyde in PBS for 20 min at room temperature. After removing the fixative, cells were next permeabilized for 60 min at room temperature with 0.1% Triton X-100 and 10% fetal calf serum (FCS) in PBS. The cells were washed once with PBS containing 1% FCS and then incubated with the primary antibody solution overnight at 4˚C. Next day, the cells were washed three times with PBS containing 1% FCS, followed by incubation with Hoechst (1:1000, 33342, Invitrogen, USA), and the secondary antibody solution at room temperature for 1.5 hour, protected from light. The cells were finally washed three times with PBS containing 1% FCS. Primary antibody solution was prepared by diluting mouse anti-tubulin-βIII (1:500, Cat #801201, BioLegend, USA) and rabbit anti-tyrosine hydroxylase (1:500, Cat #ab112, Abcam, UK) in PBS containing 1% FCS. Secondary antibody solution was prepared by diluting Alexa Fluor 568-conjugated goat anti-mouse IgG (1:1000, Cat #A11031, Invitrogen, USA) and Alexa Fluor 488-conjugated goat anti-rabbit IgG (1:1000, Cat #A11008, Invitrogen, USA) in PBS containing 1% FCS. Images of the stained cells were acquired using a EVOS™ FL Auto 2 Imaging System (ThermoFisher, USA).

5. Rotenone-induced neuron viability assay

For the neuron viability assay, we started a new neuron culture in a 96-well plate after propagation from 6-well plate culture. Neurons from each cell line were maintained and differentiated by following the same protocol. Matured neurons received rotenone treatment divided in different concentration groups, including 100, 200, 400, 800, 1000 and 4000 nM, together with a control and DMSO-treated group. Treatment groups had three sample replicates. After 24-hour incubation at 37 °C and 5% CO_2, 10 uL of alamarBlue™ cell viability reagent was directly added to cells in culture medium. The culture plate was then incubated for 3 hours at 37 °C and 5% CO_2, also protected from direct light. The absorbance was measured with a microplate reader Infinite M1000 (Tecan, Switzerland) at 570 nm (detection wavelength) and 600 nm (reference wavelength).

6. Bicinchoninic acid (BCA) assay for protein quantitation

The BCA protein assay was performed on the collected cell pellets according to the manufacturer's protocol (Thermo Fisher Scientific, USA). 15 mL of radio-immunoprecipitation-M (RIPA-M) assay buffer was prepared by mixing 1.5 mL of 500 mM Tris (Sigma Aldrich, USA), 1.5 mL of 1500 mM sodium chloride (NaCl), 1.5 mL 10 mM of EDTA, 0.1 mL 1 % IGEPAL CA-630 (Sigma Aldrich, USA), 30 µL protease Inhibitor Cocktail (Sigma Aldrich, USA), and compensating with Milli-Q water. 10 mL of UREA-T buffer was prepared by dissolving 4.8 g Urea with 500 µL of 1500 mM NaCl, 1 mL of 500 mM Tris, and Milli-Q water. 150 µL of ice-cold RIPA-M buffer was added to each sample pellet, which was then followed with vortexing for 10 mins, centrifuging at 16000 rcf, 4 ℃

for 10 min. The supernatant was collected into a new Eppendorf tube. Subsequently, the left-over pellet was resuspended in 75 µL of UREA-T buffer prior to vortexing, sonication for 5 min, and centrifuging at 16000 rcf and 4 °C for 10 min. The resulting supernatant was collected and combined with the previous supernatant. The final sample supernatant was obtained after vortexing and centrifuging the supernatant mixture at 16000 rcf and 4 °C for 10 min. 25 µL of standard solution or sample supernatant was added in triplicates to wells of three 96-wells plates and then added with 200 µL of working reagent in each well. The plates were covered with aluminum foil and incubated at 37 °C for 30 min. The absorbance was measured with a microplate reader Infinite M1000 (Tecan, Switzerland) at 562 nm (detection wavelength). Protein content of each sample was quantified based on a standard curve made from a series concentrations of bovine serum albumin.

7. Data processing and analysis

Metabolite peak integration was carried out using the SCIEX OS Analytics processing tool (version 2.1.6). MzQuality (https://gitlab.com/lacdr-abs/mzqualr) was used to evaluate intra-batch variations in which metabolites with a background signal over 40 % or a QC relative standard deviation over 30 % were removed. The relative abundance of the metabolite was represented with the peak area ratio of analyte to its internal standard. The peak area ratio data was first corrected by the sample protein content and normalized using probabilistic quotient method. For univariate analysis, normalized data was further treated with cube-root transformation. For multivariate analysis, normalized data was further processed with cube-root transformation and pareto scaling. Neuron viability assay obtained the sample absorbance from measurement wavelength then normalized to the absorbance from reference wavelength. The percentage of viable cells was then calculated using the sample absorbance against the average absorbance in the control group.

Statistical analysis was performed in R programming software (version 3.6.2). An independent two-tailed unpaired Student's t test was performed to evaluate the statistical difference between two treated groups, in which p-values below 0.05 were considered statistically significant. A standard Benjamini-Hochberg method was applied to control the false discovery rate for multiple hypothesis testing in the volcano analysis. Metabolites found with statistical differences were visualized in heatmap, boxplot and correlation map also implemented in R programming software (version 3.6.2).

Results

1. Mid-brain specific neuronal differentiation and its response to rotenone neurotoxicity

A successful *in vitro* iPSC-derived neuron culture is a prerequisite for our follow-up metabolomics investigation. Identification of neuron differentiation was performed at the end of the culture stage

using optical microscopy observation and immunofluorescent staining (Figure 1A-C). Positive expression of tubulin-βIII confirmed the differentiation of neurons, moreover, positive expression of tyrosine hydroxylase confirmed the presence of dopaminergic neurons (Figure 1C). The effect of rotenone concentration to induce neuronal stress but no significant neuronal death was first evaluated in this study using the alamar blue assay. Treatment with rotenone for 24 h showed a concentration-dependent decrease in the viability of mutant neurons in a visual rather than a statistical perspective (Figure 1D). Following experiments used rotenone at a medium concentration of 400 nM because there was no significant viability loss when compared to the no rotenone-treated control level.

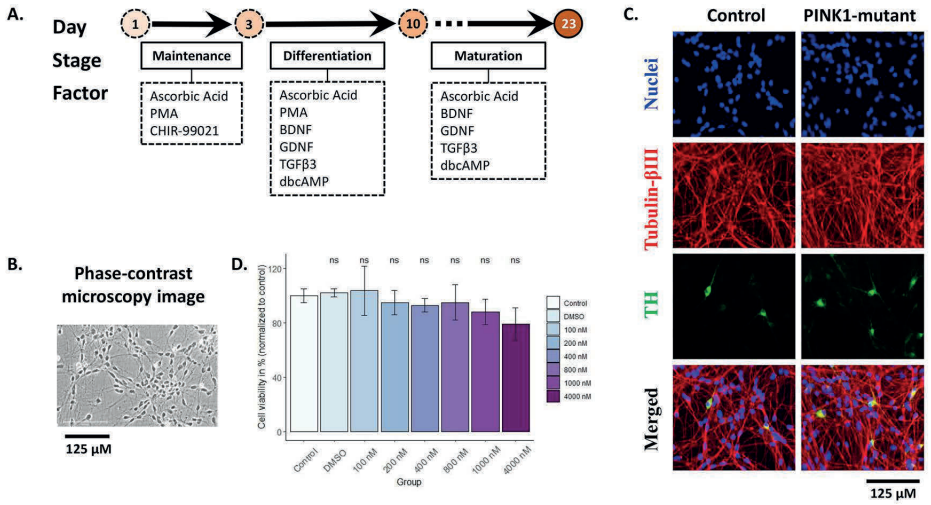

Figure 1. *In vitro* cell culture protocol overview, characterization of neuron differentiation, and viability assay with rotenone exposure. A. Differentiation of human neuroepithelial stem cells (hNESC) into midbrain-specific dopaminergic neurons. The media composition at the various stages of cell culture were shown in the below boxes. B. Neuron colony morphology in the phase-contrast microscopy image acquired on day 23, with a scale bar of 125 µm. C. Immunofluorescence characterization of isogenic PINK1-mutant (M826 cell line) and control (GC826 cell line) mature neurons. Immunofluorescence staining of mutant and isogenic control neurons showed a large percentage of tubulin-βIII expression, representing the presence of differentiated neuronal populations (red), including a population of tyrosine hydroxylase (TH) dopaminergic neurons (green), and nuclei were identified with hoechst (blue). A merged image of nuclei, tubulin-βIII and TH stains was shown at the bottom, with a scale bar of 125 µm. D. Cell viability quantification for PINK1-mutant neurons with 24-hour exposure to rotenone in a range from 100 nM to 4000 nM. Data represent means ± SE of three independent experiments, *$p < 0.05$, ns: no significant difference.

2. Metabolic disturbance in control and PINK1-mutant neurons influenced by rotenone

To characterize the individual effect of rotenone exposure or PINK1 mutation, and most importantly their joint impact on dopaminergic neuron metabolism, a combination of multiple analytical platforms was adopted to achieve a broad metabolome coverage. Targeted metabolomics analysis was performed on cell and medium samples from isogenic control groups (control/control_DMSO), a rotenone-treated control group (Rotenone), a PINK1-mutant group (PINK1) and a rotenone-treated PINK1-mutant group (PINK1_Rotenone). Heatmap visualization of individual metabolites was computed based on the relative metabolite abundance change respectively caused by rotenone exposure (Rotenone *versus* control_DMSO), PINK1 mutation (PINK1 *versus* control), or the combined influence of rotenone & PINK1 mutation (PINK1_Rotenone *versus* control_DMSO).

2.1. Central carbon metabolism

The metabolite changes were projected onto the central carbon metabolism pathways, including pathway of glycolysis, pentose phosphate pathway, tricarboxylic acid (TCA) cycle, amino acid metabolism and the connected purine & pyrimidine metabolism (Figure 2).

Lactate (LAC), as a final product of glycolysis, had significantly higher abundance in the rotenone-treated control group, PINK1-mutant group and rotenone-treated PINK1-mutant group than in the control group, suggesting an overall active glycolytic activity with either toxin or mutation influence. Significantly decreased phosphoenolpyruvate (PEP) and increased pyruvate (PYR) were also detected in the PINK1-mutant group. In contrast, increased PEP and decreased PYR were detected in the rotenone-treated control group. The fact that lactate accumulated more in the rotenone-treated group than in the PINK1-mutant group, along with the change of lactate's precursor, showed that the levels of rotenone and the PINK1 mutation's effects on active glycolysis were different, and the mutation influence was relatively minor. The other intermediate metabolites also showed interesting changes, giving a hint of the relevant enzymatic activities. The rate-limiting enzyme phosphofructokinase (PFK) can change fructose-6-phosphate (F6P) into fructose-1,6-phosphate (FDP). The precursor metabolites of F6P, particularly glucose-6-phosphate (G6P), showed a significant decrease, while the downstream metabolites of FDP, dihydroxyacetone phosphate (DHAP), glyceraldehyde 3-phosphate (G3P) showed a significant increase. The results showed an activated PFK enzymatic activity induced by either rotenone exposure or PINK1 mutation. The PINK1-mutant group showed its susceptibility to rotenone exposure reflected in the decreased level of ribose-5-phosphate (R5P), as an important intermediate metabolite of the pentose phosphate pathway. In addition, the ratio plot of NADPH/NADP+ in Figure 3 showed a significant decrease in

both rotenone-treated control/PINK1 mutant groups, further indicating an inhibitory role of rotenone on pentose phosphate pathway activity.

Opposite to the accumulation of lactate, the metabolic flux from pyruvate into acetyl coenzyme A (Acetyl-CoA) was found to be significantly decreased in both rotenone-treated control/PINK1 mutant groups. Acetyl-CoA functions as an entry into the tricarboxylic acid cycle (TCA cycle), and its decreased abundance also resulted in a decreased level of cis-aconitate (cis-ACO), α-ketoglutarate (αKG), succinate (SUC) in rotenone-treated control group. Decreased cis-ACO level was also observed in PINK1-mutant group, suggesting a reduced Acetyl-CoA oxidation in mitochondria. However, the levels of αKG, SUC, fumarate (FUM) and malate (MAL) significantly increased in the PINK1-mutant group. Moreover, an elevated αKG level was still maintained under the combined influence of rotenone&PINK1 mutation (Figure S1). We also found a significant decrease in the level of glutamine (GLN), glutamate (GLU), and its derived γ-aminobutyrate (GABA) in both rotenone-treated control/PINK1-mutant groups. Further, by looking at the ratio plot (Figure 3), the ratio of αKG/GLU showed a significant increase in the PINK1-mutant neurons and as well as in the rotenone-treated PINK1-mutant groups. These results might explain the abnormal TCA cycle in PINK1-mutant neurons was caused by an increased nutrient fueling from glutamine except glucose in response to the diversion of pyruvate towards lactate.

Compared to control group, all groups showed a significant energy reduction, reflected in the levels of ATP, UTP, GTP and CTP. Significantly elevated levels in AMP, GMP were also observed within the purine & pyrimidine metabolism. Additionally, with PINK1 mutation or rotenone exposure, elevated levels of nucleosides like guanosine, inosine, adenosine, uridine, and hypoxanthine were partially detected (Figure 2). Taken together, the disturbed neuron is more prone to degrade nucleotides than produce them by de novo synthesis due to inhibition of the pentose phosphate pathway. Strikingly, the NADH/NAD ratio increased more noticeably in the rotenone-treated control/PINK1-mutant groups than in the PINK1-mutant group alone. Overall, rotenone-treated neurons exhibited a very active glycolytic activity and nucleotide degradation, but low pentose phosphate pathway activity and TCA cycle metabolism with potentially inhibited aconitase (ACO2). PINK1-mutant neurons showed an active glycolytic activity, nucleotide degradation and disturbed TCA cycle metabolism with potentially inhibited ACO2. Furthermore, PINK1-mutant neurons showed its high sensitivity to rotenone exposure, resulting in similar metabolome alterations to mere rotenone perturbation. In addition to the major metabolome alterations found in central carbon metabolism, other amino acid changes are also interesting, such as an increased kynurenine level found in the rotenone-treated control group while a decreased

level found in the PINK1 mutant neuron, an increased tyrosine level found in rotenone-treated PINK1-mutant neurons.

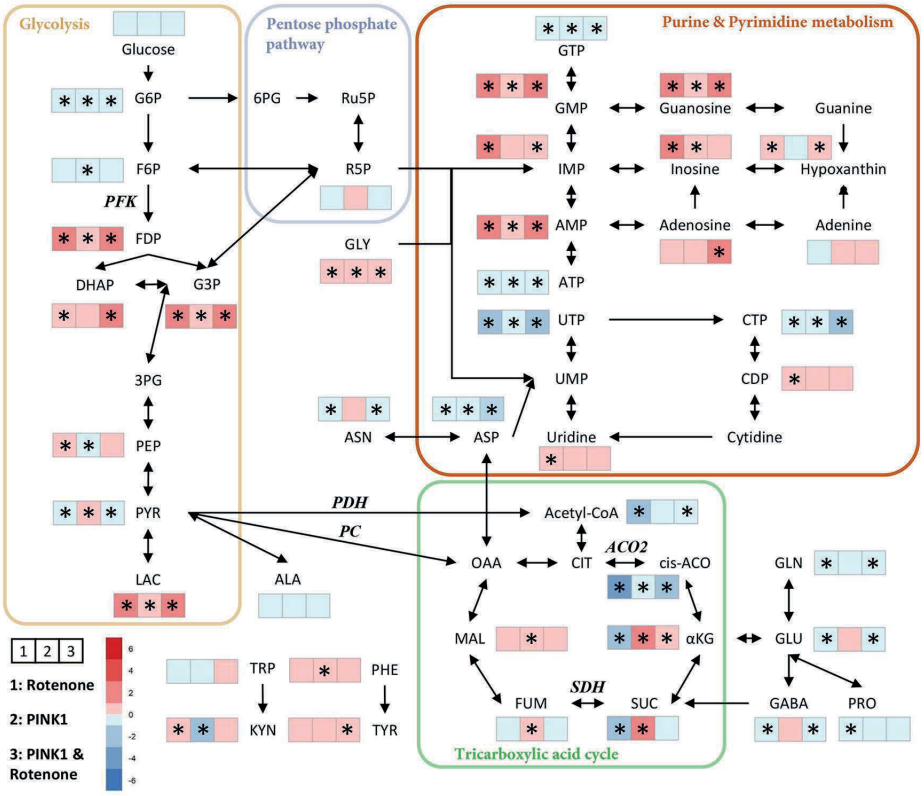

Figure 2. The metabolite alterations within central carbon metabolism, related amino acid and purine & pyrimidine metabolism, which were aroused by rotenone exposure, PINK mutation, or the combined influence of rotenone&PINK1 mutation. The resultant relative changes of each metabolites in the relevant experimental groups compared to its control group (1: rotenone-treated control group *versus* control_DMSO group; 2: PINK1-mutant group *versus* control group; 3: rotenone-treated PINK1-mutant group *versus* control_DMSO group.) were represented in a single heatmap by order from left to right. Increased or decreased change, which was calculated by the $\log_2$ fold change between the perturbed group versus the control group, was represented in red color or blue color respectively. Significant difference between group comparison was marked by an asterisk*. PFK: phosphofructokinase; PDH: Pyruvate dehydrogenase; PC: pyruvate carboxylase; SDH: succinate dehydrogenase; ACO2: aconitase.

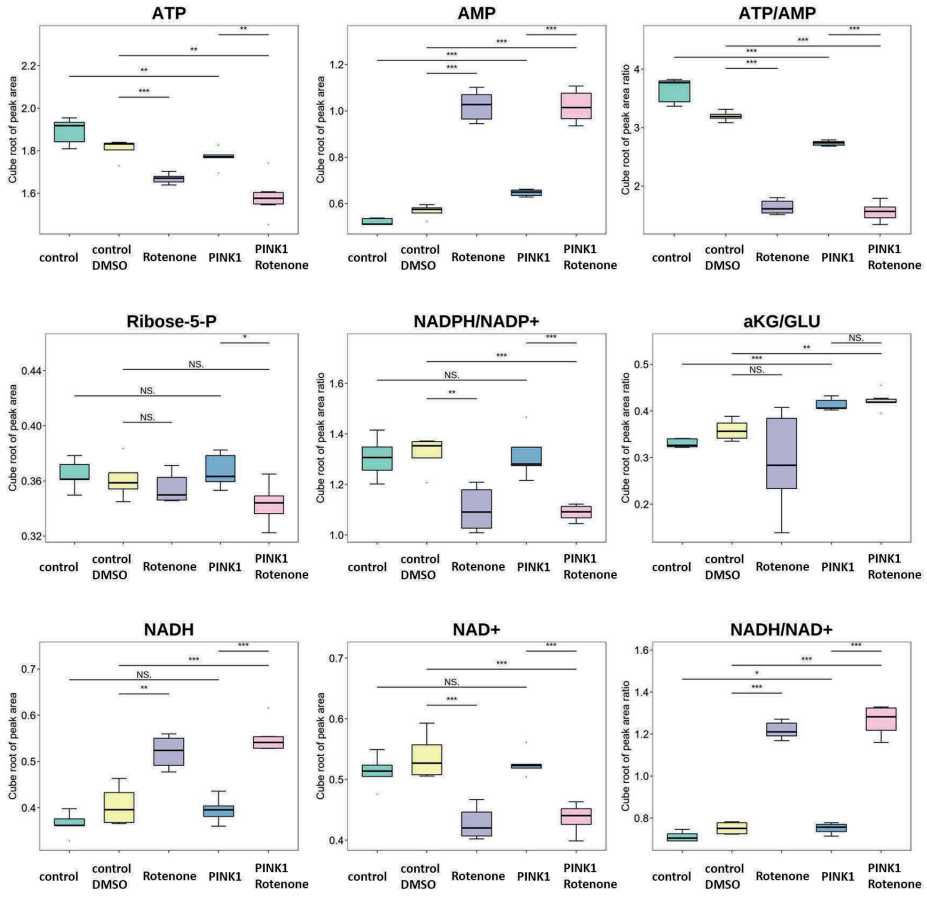

Figure 3. Box plot for showing the metabolite level of ATP, AMP, ribose-5-p, NADH, NAD+ and metabolite ratio level of ATP/AMP, NADPH/NADP+, αKG/GLU, NADH/NAD+ in control groups (control and control_DMSO), rotenone-treated control group (Rotenone), PINK1-mutant group (PINK1) and rotenone-treated PINK1-mutant group (PINK1_Rotenone). Significant difference between group comparison was marked by * ($p < 0.05$), ** ($p < 0.01$), *** ($p < 0.001$). No significant difference was marked by NS.

2.2. Acylcarnitine metabolism

When the glucose-derived energy production is limited, it might trigger neurons to utilize energy supplementation through fatty acid oxidation, which provides the electron donors to feed into the electron transport chain, powering oxidative phosphorylation and maintaining energy homeostasis [39,40]. Carnitine works as a free shuttle by forming into acylcarnitine substrates to assist long-chain fatty acid transport into mitochondria, while medium-chain fatty acid can directly permeate the inner mitochondrial membrane, as illustrated in Figure

4A. To understand more energy substrates and their linked effect to energy metabolism in PD, we also investigated the profile of acylcarnitines in all experimental groups. In total, we found 2 long-chain acylcarnitines (LCAC), 8 short-chain acylcarnitines (SCAC) that showed significant differences under the influence of rotenone or PINK1 mutation. Figure 4B showed an increased level of linoleoyl-carnitine (C18:2-carnitine) observed in rotenone-treated control/PINK1-mutant groups, and increased level of oleoyl-carnitine (C18:1-carnitine) in the PINK1-mutant group and rotenone-treated control/PINK1-mutant groups. However, a decreased free carnitine was only observed in PINK1-mutant group. Malonyl-CoA is a well-known inhibitor of carnitine palmitoyltransferase I (CPT1) [41]. Increased level of malonyl-carnitine (C3:1-2OH-carnitine) was observed along with rotenone exposure. To different extent, all the observed alterations showed an impaired capacity for long-chain fatty acid oxidation with either toxin or mutation influence. On the other hand, we found increased butyryl-carnitine (C4-carnitine) and acetyl-carnitine (C2-carnitine) with toxin or mutation influence. To compensate for the energy deficiency, neurons might have an active medium-chain fatty acid oxidation, forming into increased SCACs. Other intermediate SCACs with odd carbon atoms, such as isovaleryl-carnitine (C4-3M-carnitine), 2-methylbutyryl-carnitine (C4-2M-carnitine), propionyl-carnitine (C3-carnitine), tiglyl-carnitine (C5:1-carnitine), methyl-malonyl-carnitine (C3-DC-M-carnitine) are products derived from branched chain amino acid metabolism. As another nutrient fueling to TCA cycle, branched chain amino acids (leucine, isoleucine and valine) provide carbons to support forming into products of acetyl-CoA and succinate. A significant decreased levels of these SCACs suggested less utilization of branched chain amino acids for energy production (Figure 4C) [42].

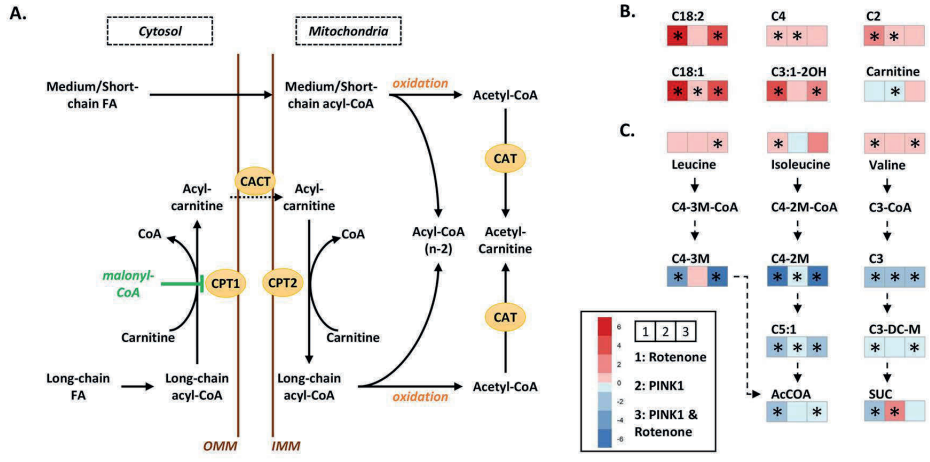

Figure 4. Metabolic disturbances associated with acylcarnitine metabolism in control and PINK1 mutant neurons influenced by rotenone. A. Illustration of mitochondrial fatty acid β-oxidation in neurons. CPT1: carnitine palmitoyltransferase I; CPT2: carnitine palmitoyltransferase II; CACT: carnitine-acylcarnitine translocase. B. Metabolite heatmap showing the relative changes of linoleoyl-carnitine (C18:2-carnitine), oleoyl-carnitine (C18:1-carnitine), malonyl-carnitine (C3:1-2OH-carnitine), butyryl-carnitine (C4-carnitine) and acetyl-carnitine (C2-carnitine) in three experimental groups compared to the control group (1: rotenone-treated control group *versus* control_DMSO group; 2: PINK1-mutant group *versus* control group; 3: rotenone-treated PINK1-mutant group *versus* control_DMSO group.). C. Metabolite heatmap showing the relative change of isovaleryl-carnitine (C4-3M-carnitine), 2-methylbutyryl-carnitine (C4-2M-carnitine), propionyl-carnitine (C3-carnitine), tiglyl-carnitine (C5:1-carnitine), methyl-malonyl-carnitine (C3-DC-M-carnitine) in three experimental groups compared to the control group. Increased or decreased change, which was calculated by the $\log_2$ fold change between the perturbed group *versus* the control group, was represented in red color or blue color respectively. Significant difference between group comparison was marked by an asterisk*.

3.2.3. Signaling lipid mediators

More than energy balance, fatty acids also play distinct roles in neuroinflammatory regulation, especially poly unsaturated fatty acids (PUFA) and their bioactive eicosanoid and docosanoid metabolites [43]. To investigate further into alterations associated with neuroinflammation in the situation of energy deficiency, we examined PUFAs and signaling lipid mediators secreted into medium samples from all experimental groups. Figure 5A showed an illustrated pathway for the lipid mediators' derivation from the turnover of membrane phospholipids. Among 40 metabolites detected, Figure 5B depicts the metabolite differences observed for PUFAs-n3, PUFAs-n6, PUFAs-n9 and their derived 10 lipid mediators. In the free PUFA group, gamma-linolenic acid (GLA, C18:3, n6), arachidonic acid (AA, C20:4, n6), eicosapentaenoic acid (EPA, C20:5, n3) showed significant increased levels in not only in individual-factor but also in joint-factor group. Interestingly, significantly decreased adrenic acid (AdA, C22:4, n6), docosapentaenoic acid (DPA, C22:5, n6) and increased docosahexaenoic acid (DHA, C22:6, n3) was shown in the PINK1-mutant group. In contrast, the opposite expression of DPA was shown in the rotenone-treated control group. Several signaling lipid mediators were detected with significant alterations from enzymatic-oxidation of linoleic acid (LA, C18:2, n6), AA, EPA and DHA via cytochrome P450 (CYP), cyclooxygenase (COX), lipoxygenase (LOX) or auto-oxidation. A ratio plot can better explain the oxidative metabolism. As can be seen in Figure 6, an increased trend in the ratios of 9,10,13-TriHOME/LA, 9,12,13-TriHOME/LA and 13-HODE/LA, while a decreased level in the ratio of 16-HDoHE/DHA were observed in

individual-factor and joint-factor group. The results suggested an active LOX- and COX-mediated oxidation of LA compared to an inactive DHA oxidation. On the other hand, decreased ratio of 14,15-DiHETrE/AA, 14,15-DiHETE/EPA, 5-HEPE/EPA and 9-HEPE/EPA was only found in rotenone-treated control/PINK1-mutated groups. By analyzing the oxidative stress in neurons with the indicators of glutathione (GSH) and ascorbic acid, we found a similar expression pattern, especially for the rotenone-treated control/PINK1-mutant groups. A correlation analysis between lipid mediators and antioxidant markers (GSH, ascorbic acid, NADPH/NADP+) further explored the relationship between oxidative stress and PUFA oxidations (Figure 7). We found a strong positive correlation of antioxidants to AA-, EPA- and DHA-derived oxylipins, while a strong negative correlation to LA-derived oxylipins. Decrease in antioxidants indicates an increased oxidative stress, which may cause an overactive peroxidation of LA in comparison to the other PUFAs.

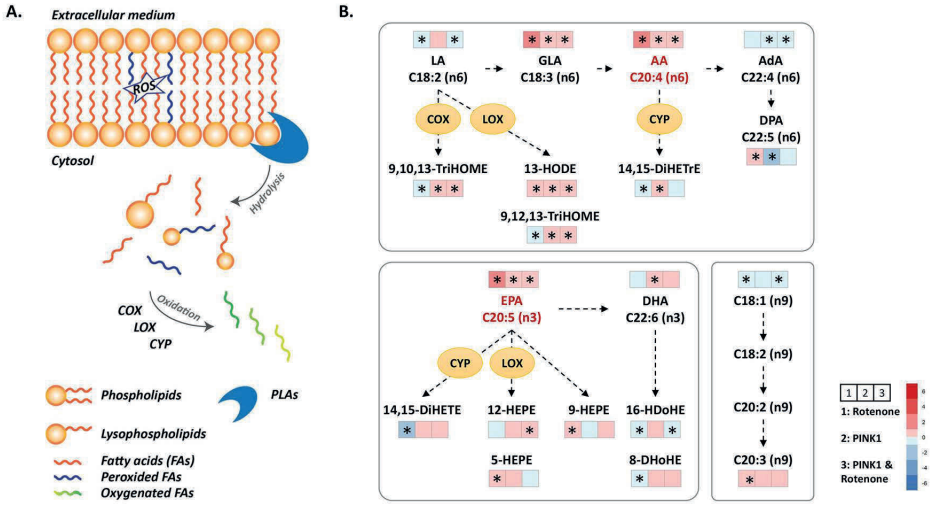

Figure 5. Metabolic disturbances associated with poly unsaturated fatty acid (PUFA) metabolism in control and PINK1 mutant neurons influenced by rotenone. A. An illustration of the production of free PUFAs in neurons from membrane phospholipids upon stimulation of the enzyme phospholipase A (PLA) by oxidative stress. Three main enzymatic pathways are responsible for the formation of eicosanoid and docosanoid metabolites, involving cyclooxygenases (COXs), lipoxygenases (LOXs), and epoxygenases of the cytochrome P-450 family (CYPs). ROS: reactive oxygen species. B. Metabolite heatmap showing the relative change of PUFAs and their derived lipid mediators in three experimental groups compared to the control group (1: rotenone-treated control group *versus* control_DMSO group; 2: PINK1-mutant group *versus* control group; 3: rotenone-treated PINK1-mutant group *versus* control_DMSO group.). Increased or decreased change, which was calculated

by the $\log_2$ fold change between the perturbed group versus the control group, was represented in red color or blue color respectively. Significant differences between group comparisons were marked by an asterisk*.

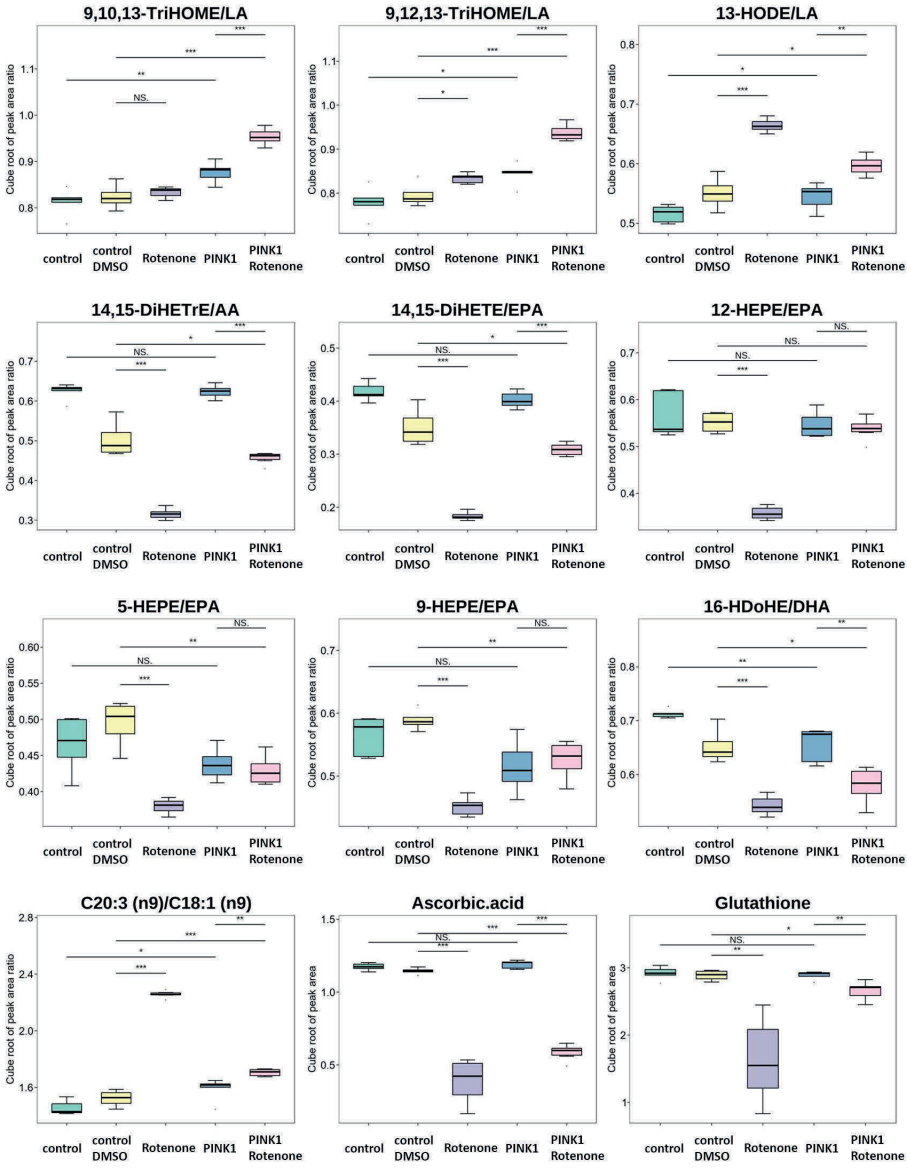

Figure 6. Metabolite ratio changes representing PUFA oxidation, antioxidant metabolite changes in control and PINK1 mutant neurons influenced by rotenone. Box plot for showing the metabolite ratio levels associated with PUFA metabolism in control groups (control and control_DMSO), rotenone-

treated control group (Rotenone), PINK1-mutant group (PINK1) and rotenone-treated PINK1-mutant group (PINK1_Rotenone). Significant difference between group comparison was marked by * ($p < 0.05$), ** ($p < 0.01$), *** ($p < 0.001$). No significant difference was marked by NS.

Figure 7. The correlation heatmap represents pairwise Pearson correlations between the metabolite features from (Figure 6) across all the experimental and control groups. The circle size is proportional to the absolute values of the correlation coefficients. One asterisk was added to encode significance of the correlation. Green indicates a positive correlation, while purple reveals a negative correlation. A darker color indicates a higher degree of positive or negative correlation.

3. Metabolic profiling for showing energy restoration by NAD+ treatment

NAD+ is reported as an energy supplementing molecule that has been implemented as a PD treatment in many clinical trials so far [44]. To investigate the impact of NAD+ treatment on our neurodegenerative models caused by PINK1 mutation or joint factors, we further examined metabolite changes of the energy, acylcarnitines and signaling lipids metabolism in the NAD-treated neurons. In the partial least squares-discriminant analysis (PLS-DA) (Figure 8A), the set of control/control_DMSO, control_rotenone and control_rotenone_NAD groups showed clear separations, similarly, PINK1/PINK1_DMSO/PINK1_NAD, PINK1_rotenone and PINK1_rotenone_NAD groups also revealed clear separations. The rotenone-treated control/PINK1-mutant groups

greatly differed from the control groups. Interestingly, their NAD+-treated groups colored in red and grey respectively showed a shift towards their correspondent control groups. The PINK1_NAD group hardly showed separation from the PINK1 group. Based on the volcano analysis between PINK1_NAD and PINK1 group, only one metabolite, hypoxanthine, was found as increased after treatment (Figure 8B). While totally 53 metabolites were found as changed after treating the control_rotenone group. (Figure 8C, Table S5), and 29 metabolites were found to be changed after treating the PINK1_rotenone group (Figure 8D, Table S5). 18 metabolites were found commonly changed in both control_rotenone_NAD group and PINK1_rotenone_NAD group.

To figure out whether the above found metabolite changes were caused by a positive treatment effect or side effect by NAD+, we next performed a heatmap analysis for these 18 metabolites in the context also including control groups of control/control_DMSO and PINK1/PINK1_DMSO. As shown in Figure 8E, the level of sorbitol, lactate, AMP, malonylcarnitine, 9,12,13-triHOME, 9,10,13-triHOME and 13-HODE reduced significantly in the NAD+ treated-groups, as well as towards the control group level. On the other hand, ascorbic acid, cis-aconitate, NAD+, propionylcarnitine, tiglylcarnitine, isovalerylcarnitine, 2-methylbutyroylcarnitine, 14,15-diHETE and 14,15-diHETrE were found increased significantly, also close to the control group level. In addition, ratio box plots in Figure S2 clearly depicted changed LA oxidation and AA oxidation after NAD+ treatment, as shown in the decreased level of 9,10,13-TriHOME/LA, 9,12,13-TriHOME/LA and 13-HODE/LA and increased level of 14,15-DiHETrE/AA. The heatmap results suggested NAD+ supplementation causes a downregulated glycolytic activity, upregulated branched chain amino acid metabolism and altered fatty acid oxidation. An activated oxidative phosphorylation in mitochondria can be further indicated by the elevated levels of ATP/AMP, GTP/GMP and decreased level of NADH/NAD+ observed upon NAD+ treatment for rotenone-treated group (Figure 9). Nevertheless, continuously increased IMP and AA (C20:4, n6) in response to NAD+ supplementation and a decreased level in the ratio of NADPH/NADP+ in NAD+-treated PINK1 mutant group might indicate a potential side effect.

A second heatmap analysis was made for those unique metabolites only found to be changed in the PINK1_rotenone_NAD group (Figure 8F). Leucine, betaine, valine, tyrosine, adenosine, oleic acid (C18:1, n9) and 12-HEPE decreased significantly, changing towards the control PINK1/PINK1_DMSO group level, while NADP+, mead acid (MA, C20:3, n9), dihomo-gamma-linolenic acid (DGLA, C20:3, n6) and DPA (C22:5, n6) were found increased significantly, but further away from the control level. An increased utilization of branched chain amino acids matched the aforementioned discovery. However, the results

of a further decreased oxidation of EPA into 12-HEPE/5-HEPE and a further increased MA metabolism were unexpected (Figure S2).

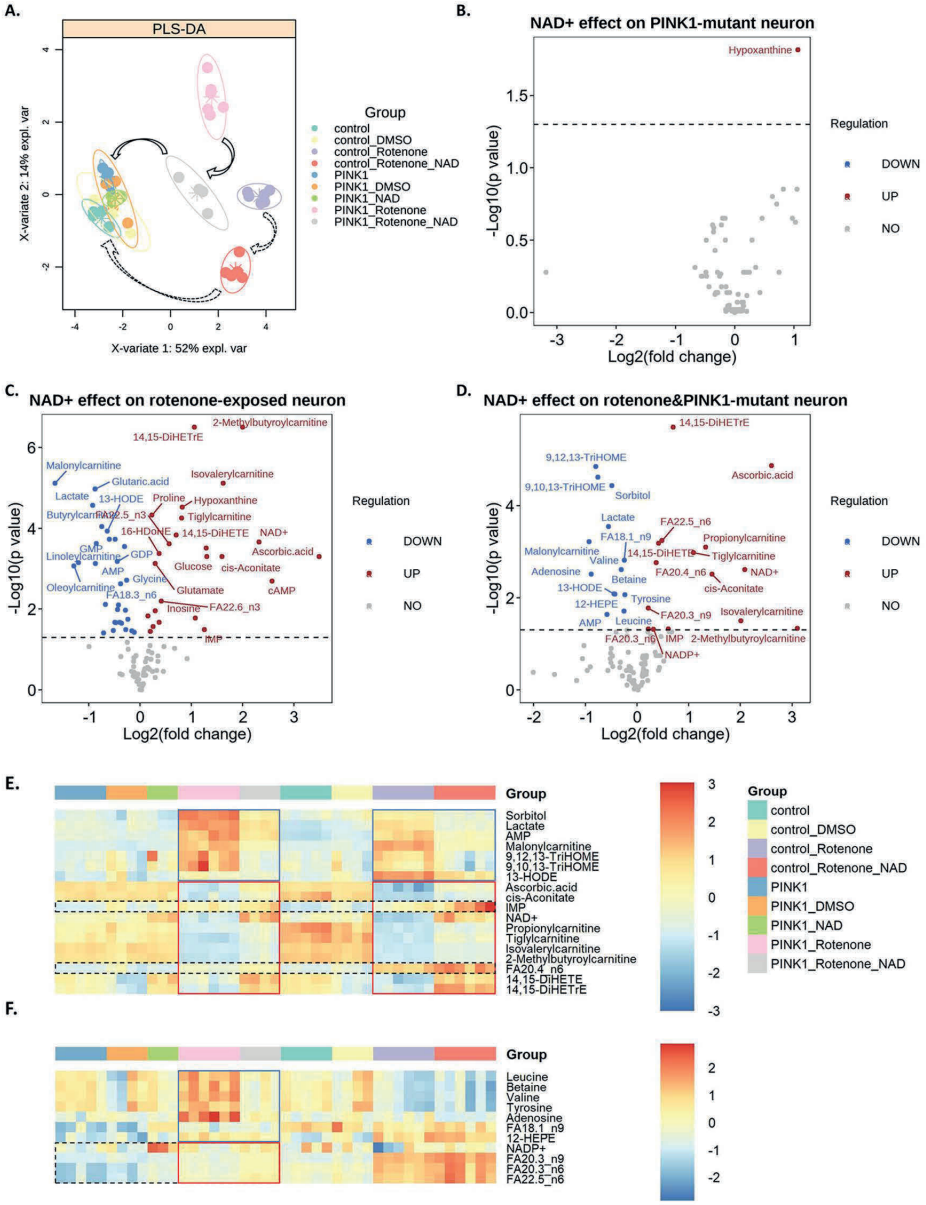

Figure 8. Impacts of NAD+ treatment on cellular metabolome in control and PINK1 mutant neurons influenced by rotenone. A. PLS-DA score plot reflecting statistical separation between all perturbation, treatment and control groups. B-D. Volcano plot analysis between PINK1_NAD and PINK1groups

(B), control_rotenone_NAD and control_rotenone groups (C), PINK1_rotenone_NAD and PINK1_rotenone groups (D) revealing metabolite features increased and decreased by p-value and fold change analysis. Horizontal dashed lines indicate the cutoff p-value of 0.05. Metabolite features marked in red dot represent an increased level, metabolite features marked in bule dot represent a decreased level, and metabolite features marked in grey dot represent no significant difference. E, F. Heatmap profiling for metabolites that were commonly regulated in both NAD+-treated control_rotenone group and PINK1_rotenone group (E), and metabolite that were uniquely regulated in NAD+-treated PINK1_rotenone group (F).

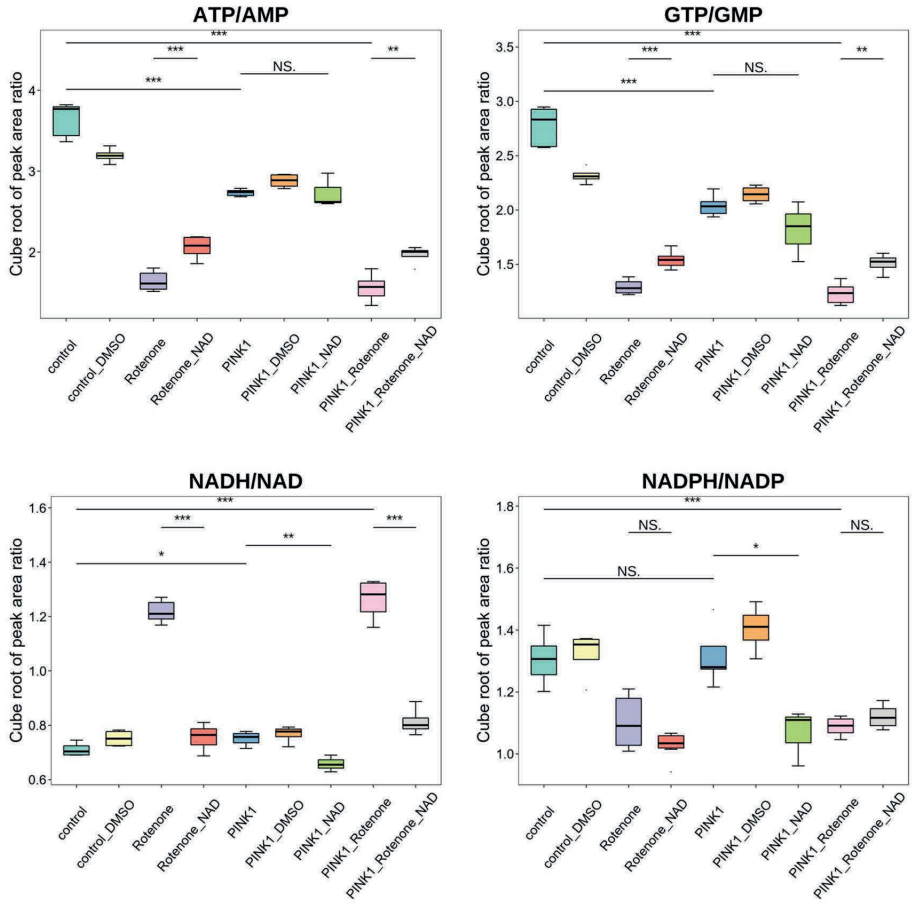

Figure 9. Box plot for showing NAD+ treatment regulation on the metabolite ratio level of ATP/AMP, GTP/GMP, NADH/NAD+ and NADPH/NADP+ for rotenone-treated control group (Rotenone), PINK1-mutant group (PINK1) and rotenone-treated PINK1-mutant group (PINK1_rotenone). Significant differences between groups were marked by * ($p < 0.05$), ** ($p < 0.01$), *** ($p < 0.001$). No significant difference was marked by NS.

Discussion

To date, very few studies were carried out on the human iPSC-derived PD-associated neuron model combined with metabolomic analysis to investigate neurodegenerative metabolism linked to multifactorial etiology. Our study reports the selective metabolomics regulation of human iPSC-derived mid-brain neurons caused by PINK1 mutation, mitochondrial complex I inhibitor (rotenone), and their joint influence. In addition, treatment efficiency via NAD+ supplementation was evaluated against in vitro cellular models of mono- and dual-cause interventions. We found similar metabolic dysregulation caused by rotenone and PINK1 mutation seen in reduced energy production and impaired redox balance, as well as differences regarding impaired mitochondrial respiration, anti-oxidative response and neuroinflammation. Neurons with inherent PINK1 mutation showed susceptibility to rotenone stimulation, resulting in more complicated neurodegenerative metabolism. Additionally, they showed insensitive response to NAD+ treatment. Considering the common and divergent alterations in metabolic pathways for the rotenone-caused and mutation-caused PD model, dual-cause interventions may play an important role in sporadic PD pathogenesis and might serve as a new strategy for in-vitro drug screening.

Energy imbalance has been regarded as a central cause leading to the progression of neurodegeneration and subsequent neuronal death in the brain substantia nigra region [45]. Reflected in the intracellular ATP level from our study, rotenone caused a much more severe and acute shutdown of energy production after 24 h, whereas PINK1 mutation exhibited a long-term and chronic energy deficiency. A high NADH/NAD+ ratio can activate pyruvate dehydrogenase kinase (PDK), leading to inhibitory phosphorylation of PDH [46]. Thus, the overall energy supply crisis can be associated with reduced acetyl-CoA utilization in the TCA cycle and an alternation towards upregulated glycolysis. Moreover, the energy deficiency failed to be compensated through branch chain amino acid metabolism and long-chain fatty acid oxidation. Medium-chain fatty acid oxidation might be upregulated for energy supplementation, however, accumulation of acetylcarnitine ultimately reflected its restricted utilization into TCA cycle.

Interestingly, TCA cycle intermediates showed complex disturbances in PINK1 mutation and rotenone-based model. Impaired mitochondrial respiration was revealed by the significantly reduced level found in cis-aconitate, which is a key TCA intermediate converted from citrate by an enzyme of aconitase. Several studies have reported a reduced aconitase activity linking to PINK1 mutation within the striatum of mice, midbrain-specific dopaminergic neurons [47,48]. Our results also found accumulation of several TCA metabolites associated with PINK1 mutation. Accumulated α-ketoglutarate, succinate, fumarate and malate could be fueled by glutamine metabolism in response to the diversion

of pyruvate towards lactate. Similar results were also reported in human iPSC-derived neurons with parkin deficiency, confirmed with ^{13}C-labeled glucose tracing [26]. Besides, an active pyruvate carboxylase through malic enzyme might be triggered by the inhibited PDH activity, which resulted in an elevated level of malate in PINK1-mutant neuron [49]. However, the impact of rotenone completely eliminated the elevated TCA activity in PINK1-mutant neurons (Figure S1). Rotenone is a classic mitochondrial complex I inhibitor that can block the oxidation of NADH to NAD+ [50]. To be noted, significantly increased NADH/NAD+ ratio levels were observed in both PINK-mutated and rotenone-treated neurons, though the rotenone effect was more pronounced than the PINK1 mutation (Figure 3). The mitochondrial complex II, also known as succinate dehydrogenase (SDH), catalyzes the oxidation of succinate to fumarate with transferring electrons to the respiratory chain ubiquinone pool [51]. In our study, the increased level of succinate, leading to a consequent decreased ratio of fumarate to succinate, was only observed in the PINK1 mutation-based model, but not in our rotenone-induced neuronal model. Gautier et.al reported a defective functional capacity on mitochondrial complex I and II in PINK1 knockout mice model [47]. Our metabolomics results supported the evidence of complex II deficiencies other than complex I associated with PINK1-mutation in neuronal model. It will be important to better elucidate the mechanism of impaired respiration in both familial and sporadic Parkinson's Disease [52].

The comprehensive metabolic changes measured in energy metabolism subsystems (glycolysis, pentose phosphate pathway, acylcarnitines, and the tricarboxylic cycle, mitochondrial oxidative phosphorylation) strongly explained a mitochondria dysfunction in both rotenone-caused and PINK1 mutation-caused PD neuronal models. Along with impaired mitochondrial respiration, complex I inhibitors also provoke excessive reactive oxygen species (ROS) production [53,54]. Defective antioxidant defense has been reported in many rotenone-induced PD models and leads to severe oxidative damage consequences [55,56]. Our data showed consistent reduced antioxidant levels of glutathione (GSH), ascorbic acid and NADPH/NADP+ ratio in the rotenone-affected neuron models, but not in the PINK1 mutant neuronal model. In another study, Testa et.al reported significant increases in oxygen-based free radicals were only observable by a moderate complex I inhibition [57]. Therefore, we believe the effect of PINK1 mutation on complex I inhibition is insufficient to induce severe damage to antioxidant defense. However, the influence of oxidative damage still remained, as supported by the changes found in PUFAs and its oxidized mediators (Figure 5), which could be related to lipid peroxidation shown in both rotenone-caused and PINK1 mutation-caused PD neuronal model. On the one hand, more PUFAs were released from cell membranes through activated phospholipases, as shown in

the significantly increased PUFAs-n3 (GLA, AA) and PUFAs-n6 (EPA). On the other hand, we also observed an increased 13-HODE, which is a reduced hydroxide generated immediately after free-radical-mediated LA oxidation via LOX enzyme and is known for inducing strong pro-inflammatory regulation [58]. In comparison to the overactive peroxidation of LA, the oxidation of other PUFAs (AA, EPA and DHA) generally exhibited a decreased activity in any rotenone-influenced models. Emerging data has demonstrated the beneficial role of 14,15-DiHETrE, an AA-derived oxylipin, in the activation of peroxisome proliferator-activated receptors and exerting anti-inflammatory effects [59,60]. Besides, omega-3 PUFA-derived hydroxy (HEPEs, HDoHEs) and dihydroxy oxylipins (DiHETEs) all showed consistently reduced levels in rotenone-influenced models. Eicosanoids derived from omega-3 PUFA generally have anti-inflammatory effects [61,62]. A recent study demonstrated the ability of EPA/DHA-derived lipid mediators to prevent the reduction in neurogenesis and the increase in neuronal apoptosis and in inflammatory transcription factors induced by pro-inflammatory cytokines [63]. Taken together with our study, these lines of evidence suggest a robust anti-inflammatory and neuroprotective system in the PINK1-mutant model, but a rather severely disturbed system caused by rotenone.

From the metabolomic perspective, NAD+ supplementation showed almost no effect on the PINK1 mutant model but wide ameliorations on metabolic dysregulation caused by rotenone toxicity. The mildly boosted mitochondrial biogenesis can be explained by the activated energy compensatory routes through branch chain amino acid metabolism and long-chain fatty acid oxidation, as NAD+ is required by both processes as a key cofactor. It also showed ameliorations in the rotenone-induced inflammatory response from pro-inflammatory towards anti-inflammatory. Apart from this, the dual-cause model manifested more unexpected side effects in the PUFAs metabolism, such as decreased EPA-derived HEPEs, increased omega-6 PUFAs and increased oleic acid metabolism into mead acid. To be noted, mead acid is a classic marker for essential fatty acid deficiency in mammalian cell culture [64]. Its presence also suggests an abnormal cell membrane with inadequate supply of AA and DHA, and has the potential consequences of loss of integrity and increased risk of rupture [65]. These unexpected changes can be likely associated with the PINK1 mutation. Overall, the evaluation of NAD treatment proves to have a limited rescuing ability in retrieving energy failure caused by complex I inhibition, but not effective for PINK1 mutant neurons. However, our study has its limitations in exploring NAD+ treatment effect only within a 24-hour time range rather than a long-term effect. Future studies can explore the potential prevention benefits for boosting the capacity of neuron against toxin intervention via long-term NAD+ or other NAD+ precursor supplementation, such as niacin

[66], nicotinamide riboside [67]. In addition, this study was performed based on the PINK1 mutant and gene-corrected hNESC cell lines derived from one patient. A large study involving multiple patients should be performed to validate current discoveries.

Conclusions

In summary, our study elucidated a comprehensive picture of metabolomic dysregulation in an in vitro iPSC-derived neuronal model of PD represented by the PINK1 mutation, mitochondrial complex I inhibitor (rotenone), and joint-factor intervention. Based on the characteristic changes related to energy metabolism and oxidative stress, we clearly address the molecular mechanism of mitochondrial dysfunction in the pathogenesis of PD. Especially with the distinct responses in neuronal antioxidation and inflammation aroused by genome or environmental toxin intervention, the complexity of sporadic PD is further revealed. These findings further support a rising hypothesis, that endogenous PINK1 mutation interacting with exogenous stress can result in converged pathogenetic pathway changes towards parkinsonism. Discoveries in the disturbed pathway changes can help explore more potential therapeutic targets. Moreover, our study targeted the energy decline reflected in the decreased NAD+ level. For the first time, our findings showed that supplementing NAD+ ameliorated rotenone-related energy defects, but had no effect in the case of PINK1 mutation. Instead, it brought unexpected PUFA dysregulation to the dual-factor group. Future improvements can still be made in regards of utilizing the stable-isotope labeling technique for tracing interesting pathways in order to gain more accurate insights on metabolic flux regulation at a dynamic level.

Acknowledgments

We would like to greatly thank Matthijs Vlasveld and Sylvia Le Dévédec for their support in neuron viability assay. L. Huang would like to thank the financial support from China Scholarship Council (CSC) Grant [No. 201806210057]. This project received funding from the European Union's Horizon 2020 research and innovation programme, for the SysMedPD project, under grant agreement No. 668738, the Dutch National Institutes of Health (ZonMw) TKI-LSH Neuromet project (LSHM18092) and the Dutch Research Council (NWO) 'Investment Grant NWO Large' program, for the 'Building the infrastructure for Exposome re-search: Exposome-Scan' project (No. 175.2019.032).

References

1. Dauer W, Przedborski S. Parkinson's Disease: Mechanisms and Models. Neuron. 2003;39:889–909.
2. Kouli A, Torsney KM, Kuan W-L. Parkinson's Disease: Etiology, Neuropathology, and Pathogenesis. Exon Publications. 2018;3–26.
3. Schapira AH, Jenner P. Etiology and pathogenesis of Parkinson's disease. Movement Disorders. 2011;26:1049–55.
4. Farrer MJ. Genetics of Parkinson disease: paradigm shifts and future prospects. Nature Reviews Genetics. 2006;7:306–18.

5. Bentivoglio AR, Cortelli P, Valente EM, Ialongo T, Ferraris A, Elia A, et al. Phenotypic characterisation of autosomal recessive PARK6-linked parkinsonism in three unrelated Italian families. Movement Disorders. 2001;16:999–1006.
6. Valente EM, Brancati F, Caputo V, Graham EA, Davis MB, Ferraris A, et al. PARK6 is a common cause of familial parkinsonism. Neurol Sci. 2002;23:s117–8.
7. Reed X, Bandrés-Ciga S, Blauwendraat C, Cookson MR. The role of monogenic genes in idiopathic Parkinson's disease. Neurobiology of Disease. 2019;124:230–9.
8. Zhou H, Falkenburger BH, Schulz JB, Tieu K, Xu Z, Xia XG. Silencing of the Pink1 Gene Expression by Conditional RNAi Does Not Induce Dopaminergic Neuron Death in Mice. Int J Biol Sci. 2007;3:242–50.
9. Kitada T, Pisani A, Porter DR, Yamaguchi H, Tscherter A, Martella G, et al. Impaired dopamine release and synaptic plasticity in the striatum of PINK1-deficient mice. Proceedings of the National Academy of Sciences. Proceedings of the National Academy of Sciences; 2007;104:11441–6.
10. Tanner CM, Kamel F, Ross GW, Hoppin JA, Goldman SM, Korell M, et al. Rotenone, paraquat, and Parkinson's disease. Environ Health Perspect. 2011;119:866–72.
11. Martinez TN, Greenamyre JT. Toxin Models of Mitochondrial Dysfunction in Parkinson's Disease. Antioxid Redox Signal. 2012;16:920–34.
12. Haque ME, Mount MP, Safarpour F, Abdel-Messih E, Callaghan S, Mazerolle C, et al. Inactivation of Pink1 Gene in Vivo Sensitizes Dopamine-producing Neurons to 1-Methyl-4-phenyl-1,2,3,6-tetrahydropyridine (MPTP) and Can Be Rescued by Autosomal Recessive Parkinson Disease Genes, Parkin or DJ-1. Journal of Biological Chemistry. Elsevier; 2012;287:23162–70.
13. Castro IP de, Martins LM, Tufi R. Mitochondrial quality control and neurological disease: an emerging connection. Expert Reviews in Molecular Medicine. Cambridge University Press; 2010;12:e12.
14. Holmes E, Wilson ID, Nicholson JK. Metabolic Phenotyping in Health and Disease. Cell. Elsevier; 2008;134:714–7.
15. Beger RD, Dunn W, Schmidt MA, Gross SS, Kirwan JA, Cascante M, et al. Metabolomics enables precision medicine: "A White Paper, Community Perspective." Metabolomics. 2016;12:149.
16. Lu Z, Wang J, Li M, Liu Q, Wei D, Yang M, et al. (1)H NMR-based metabolomics study on a goldfish model of Parkinson's disease induced by 1-methyl-4-phenyl-1,2,3,6-tetrahydropyridine (MPTP). Chem Biol Interact. 2014;223:18–26.
17. Anandhan A, Lei S, Levytskyy R, Pappa A, Panayiotidis MI, Cerny RL, et al. Glucose Metabolism and AMPK Signaling Regulate Dopaminergic Cell Death Induced by Gene (α-Synuclein)-Environment (Paraquat) Interactions. Mol Neurobiol. 2017;54:3825–42.
18. Tyurina YY, Polimova AM, Maciel E, Tyurin VA, Kapralova VI, Winnica DE, et al. LC/MS analysis of cardiolipins in substantia nigra and plasma of rotenone-treated rats: implication for mitochondrial dysfunction in Parkinson's disease. Free Radic Res. 2015;49:681–91.
19. Gao H-C, Zhu H, Song C-Y, Lin L, Xiang Y, Yan Z-H, et al. Metabolic Changes Detected by Ex Vivo High Resolution 1H NMR Spectroscopy in the Striatum of 6-OHDA-Induced Parkinson's Rat. Mol Neurobiol. 2013;47:123–30.
20. Shukla AK, Ratnasekhar Ch, Pragya P, Chaouhan HS, Patel DK, Chowdhuri DK, et al. Metabolomic Analysis Provides Insights on Paraquat-Induced Parkinson-Like Symptoms in Drosophila melanogaster. Mol Neurobiol. 2016;53:254–69.
21. Zheng H, Zhao L, Xia H, Xu C, Wang D, Liu K, et al. NMR-Based Metabolomics Reveal a Recovery from Metabolic Changes in the Striatum of 6-OHDA-Induced Rats Treated with Basic Fibroblast Growth Factor. Mol Neurobiol. 2016;53:6690–7.
22. Rappley I, Myers DS, Milne SB, Ivanova PT, Lavoie MJ, Brown HA, et al. Lipidomic profiling in mouse brain reveals differences between ages and genders, with smaller changes associated with alpha-synuclein genotype. J Neurochem. 2009;111:15–25.
23. Chen X, Xie C, Sun L, Ding J, Cai H. Longitudinal Metabolomics Profiling of Parkinson's Disease-Related α-Synuclein A53T Transgenic Mice. PLoS One. 2015;10:e0136612.
24. Baykal AT, Jain MR, Li H. Aberrant regulation of choline metabolism by mitochondrial electron transport system inhibition in neuroblastoma cells. Metabolomics. 2008;4:347–56.
25. Lei S, Zavala-Flores L, Garcia-Garcia A, Nandakumar R, Huang Y, Madayiputhiya N, et al. Alterations in energy/redox metabolism induced by mitochondrial and environmental toxins: a specific role for glucose-6-phosphate-dehydrogenase and the pentose phosphate pathway in paraquat toxicity. ACS Chem Biol. 2014;9:2032–48.
26. Okarmus J, Havelund JF, Ryding M, Schmidt SI, Bogetofte H, Heon-Roberts R, et al. Identification of bioactive metabolites in human iPSC-derived dopaminergic neurons with PARK2 mutation: Altered mitochondrial and energy metabolism. Stem Cell Reports. 2021;16:1510–26.
27. Wang W, Zhao F, Ma X, Perry G, Zhu X. Mitochondria dysfunction in the pathogenesis of Alzheimer's disease: recent advances. Molecular Neurodegeneration. 2020;15:30.
28. Fang EF, Lautrup S, Hou Y, Demarest TG, Croteau DL, Mattson MP, et al. NAD + in Aging: Molecular Mechanisms and Translational Implications. Trends in Molecular Medicine. 2017;23:899–916.
29. Lautrup S, Sinclair DA, Mattson MP, Fang EF. NAD+ in Brain Aging and Neurodegenerative Disorders. Cell Metabolism. 2019;30:630–55.
30. Brakedal B, Dölle C, Riemer F, Ma Y, Nido GS, Skeie GO, et al. The NADPARK study: A randomized phase I trial of nicotinamide riboside supplementation in Parkinson's disease. Cell Metabolism. 2022;34:396-407.e6.

31. Radenkovic D, Reason, Verdin E. Clinical Evidence for Targeting NAD Therapeutically. Pharmaceuticals (Basel). 2020;13:247.
32. Moreno EL, Hachi S, Hemmer K, Trietsch SJ, Baumuratov AS, Hankemeier T, et al. Differentiation of neuroepithelial stem cells into functional dopaminergic neurons in 3D microfluidic cell culture. Lab on a Chip. 2015;15:2419–28.
33. Reinhardt P, Glatza M, Hemmer K, Tsytsyura Y, Thiel CS, Höing S, et al. Derivation and Expansion Using Only Small Molecules of Human Neural Progenitors for Neurodegenerative Disease Modeling. Daadi M, editor. PLoS ONE. 2013;8:e59252.
34. Preciat G, Moreno EL, Wegrzyn AB, Willacey CCW, Modamio J, Monteiro FL, et al. Mechanistic model-driven exometabolomic characterisation of human dopaminergic neuronal metabolism [Internet]. bioRxiv; 2021 [cited 2022 Oct 15]. p. 2021.06.30.450562.
35. Huang L, Drouin N, Causon J, Wegrzyn A, Castro-Perez J, Fleming R, et al. Reconstruction of Glutathione Metabolism in the Neuronal Model of Rotenone-Induced Neurodegeneration Using Mass Isotopologue Analysis with Hydrophilic Interaction Liquid Chromatography-Zeno High-Resolution Multiple Reaction Monitoring. Anal Chem. 2023;95:3255–66.
36. Zazzo A. Signaling lipids as diagnostic biomarkers for ocular surface cicatrizing conjunctivitis. J Mol Med. 2020;10.
37. Hosseinkhani F, Huang L, Dubbelman A-C, Guled F, Harms AC, Hankemeier T. Systematic Evaluation of HILIC Stationary Phases for Global Metabolomics of Human Plasma. Metabolites. 2022;12:165.
38. Alves RDAM, Dane AD, Harms A, Strassburg K, Seifar RM, Verdijk LB, et al. Global profiling of the muscle metabolome: method optimization, validation and application to determine exercise-induced metabolic effects. Metabolomics. 2015;11:271–85.
39. McCann MR, George De la Rosa MV, Rosania GR, Stringer KA. L-Carnitine and Acylcarnitines: Mitochondrial Biomarkers for Precision Medicine. Metabolites. 2021;11:51.
40. Jones LL, McDonald DA, Borum PR. Acylcarnitines: role in brain. Prog Lipid Res. 2010;49:61–75.
41. Knottnerus SJG, Bleeker JC, Wüst RCI, Ferdinandusse S, IJlst L, Wijburg FA, et al. Disorders of mitochondrial long-chain fatty acid oxidation and the carnitine shuttle. Rev Endocr Metab Disord. 2018;19:93–106.
42. Chen W-S, Liu M-H, Cheng M-L, Wang C-H. Decreases in Circulating Concentrations of Short-Chain Acylcarnitines are Associated with Systolic Function Improvement After Decompensated Heart Failure. International Heart Journal. 2020;61:1014–21.
43. Liu JJ, Green P, John Mann J, Rapoport SI, Sublette ME. Pathways of polyunsaturated fatty acid utilization: Implications for brain function in neuropsychiatric health and disease. Brain Research. 2015;1597:220–46.
44. Radenkovic D, Reason, Verdin E. Clinical Evidence for Targeting NAD Therapeutically. Pharmaceuticals (Basel). 2020;13:247.
45. Błaszczyk JW. The Emerging Role of Energy Metabolism and Neuroprotective Strategies in Parkinson's Disease. Front Aging Neurosci. 2018;10:301.
46. Houten SM, Wanders RJA. A general introduction to the biochemistry of mitochondrial fatty acid β-oxidation. Journal of Inherited Metabolic Disease. 2010;33:469–77.
47. Gautier CA, Kitada T, Shen J. Loss of PINK1 causes mitochondrial functional defects and increased sensitivity to oxidative stress. Proceedings of the National Academy of Sciences. 2008;105:11364–9.
48. Bus C, Zizmare L, Feldkaemper M, Geisler S, Zarani M, Schaedler A, et al. Human Dopaminergic Neurons Lacking PINK1 Exhibit Disrupted Dopamine Metabolism Related to Vitamin B6 Co-Factors. iScience. 2020;23:101797.
49. Hassel B. Pyruvate carboxylation in neurons. Journal of Neuroscience Research. 2001;66:755–62.
50. Alam M, Schmidt WJ. Rotenone destroys dopaminergic neurons and induces parkinsonian symptoms in rats. Behavioural Brain Research. 2002;136:317–24.
51. Rustin P, Munnich A, Rötig A. Succinate dehydrogenase and human diseases: new insights into a well-known enzyme. Eur J Hum Genet. Nature Publishing Group; 2002;10:289–91.
52. Plun-Favreau H, Hardy J. PINK1 in mitochondrial function. Proceedings of the National Academy of Sciences. Proceedings of the National Academy of Sciences; 2008;105:11041–2.
53. Sipos I, Tretter L, Adam-Vizi V. Quantitative relationship between inhibition of respiratory complexes and formation of reactive oxygen species in isolated nerve terminals. J Neurochem. 2003;84:112–8.
54. Lambert AJ, Brand MD. Inhibitors of the Quinone-binding Site Allow Rapid Superoxide Production from Mitochondrial NADH:Ubiquinone Oxidoreductase (Complex I) *. Journal of Biological Chemistry. Elsevier; 2004;279:39414–20.
55. Neely MD, Davison CA, Aschner M, Bowman AB. From the Cover: Manganese and Rotenone-Induced Oxidative Stress Signatures Differ in iPSC-Derived Human Dopamine Neurons. Toxicol Sci. 2017;159:366–79.
56. Sherer TB, Betarbet R, Testa CM, Seo BB, Richardson JR, Kim JH, et al. Mechanism of Toxicity in Rotenone Models of Parkinson's Disease. J Neurosci. 2003;23:10756–64.
57. Testa CM, Sherer TB, Greenamyre JT. Rotenone induces oxidative stress and dopaminergic neuron damage in organotypic substantia nigra cultures. Molecular Brain Research. 2005;134:109–18.
58. Petrovic S, Arsic A, Ristic-Medic D, Cvetkovic Z, Vucic V. Lipid Peroxidation and Antioxidant Supplementation in Neurodegenerative Diseases: A Review of Human Studies. Antioxidants. Multidisciplinary Digital Publishing Institute; 2020;9:1128.

59. Gervois P, Fruchart J-C, Delerive P, Staels B. Induction of IκBα Expression as a Mechanism Contributing to the Anti-inflammatory Activities of Peroxisome Proliferator-activated Receptor-α Activators*. Journal of Biological Chemistry. 2000;275:36703–7.

60. Fang X, Hu S, Xu B, Snyder GD, Harmon S, Yao J, et al. 14,15-Dihydroxyeicosatrienoic acid activates peroxisome proliferator-activated receptor-α. American Journal of Physiology-Heart and Circulatory Physiology. American Physiological Society; 2006;290:H55–63.

61. Kopecky J, Rossmeisl M, Flachs P, Kuda O, Brauner P, Jilkova Z, et al. n-3 PUFA: bioavailability and modulation of adipose tissue function: Symposium on 'Frontiers in adipose tissue biology.' Proceedings of the Nutrition Society. Cambridge University Press; 2009;68:361–9.

62. Echeverría F, Ortiz M, Valenzuela R, Videla LA. Long-chain polyunsaturated fatty acids regulation of PPARs, signaling: Relationship to tissue development and aging. Prostaglandins, Leukotrienes and Essential Fatty Acids. 2016;114:28–34.

63. Borsini A, Nicolaou A, Camacho-Muñoz D, Kendall AC, Di Benedetto MG, Giacobbe J, et al. Omega-3 polyunsaturated fatty acids protect against inflammation through production of LOX and CYP450 lipid mediators: relevance for major depression and for human hippocampal neurogenesis. Mol Psychiatry. Nature Publishing Group; 2021;26:6773–88.

64. Ichi I, Kono N, Arita Y, Haga S, Arisawa K, Yamano M, et al. Identification of genes and pathways involved in the synthesis of Mead acid (20:3n−9), an indicator of essential fatty acid deficiency. Biochimica et Biophysica Acta (BBA) - Molecular and Cell Biology of Lipids. 2014;1841:204–13.

65. Crawford MA, Golfetto I, Ghebremeskel K, Min Y, Moodley T, Poston L, et al. The potential role for arachidonic and docosahexaenoic acids in protection against some central nervous system injuries in preterm infants. Lipids. 2003;38:303–15.

66. Alisky JM. Niacin improved rigidity and bradykinesia in a Parkinson's disease patient but also caused unacceptable nightmares and skin rash—A case report. Nutritional Neuroscience. Taylor & Francis; 2005;8:327–9.

67. Schöndorf DC, Ivanyuk D, Baden P, Sanchez-Martinez A, De Cicco S, Yu C, et al. The NAD+ Precursor Nicotinamide Riboside Rescues Mitochondrial Defects and Neuronal Loss in iPSC and Fly Models of Parkinson's Disease. Cell Reports. 2018;23:2976–88.

Supplementary Materials

Table S1. Basic information of the control and diseased neural stem cell lines derived from two isogenic iPSC lines

Cell line ID	Cell type	Genotype	Study ID	Clinical diagnosis
GC826	neural stem cell	PINK1, wt/wt	Control (PINK1 gene corrected)	n/a
M826	neural stem cell	PINK1, Q456X/Q456X	PINK1 mutant	affected with Parkinson's disease

Table S2. Detected polar metabolites with ChEBI identifier, retention time and corresponding internal standards

Metabolite	Retention Time (min)	ChEBI ID	Internal standard
Leucine	2.87	25017	DL-LEUCINE-2,3,3-D3
Isoleucine	2.98	24898	DL-LEUCINE-2,3,3-D3
Taurine	3.99	15891	L-ALANINE-d3
Betaine	3.38	17750	Betaine-d9
Asparagine	4.59	22653	L-ASPARAGINE H2O (U-13C4, U15N2)
Tryptophan	2.86	27897	L-TRYPTOPHAN (U-13C11, U15N2)
Glutamine	4.48	28300	L-GLUTAMIC ACID (1,2-13C2)
GABA	3.91	16865	L-2-Aminobutyric acid-d6
Valine	3.35	27266	DL-VALINE-2,3,4,4,5,5-D8
Proline	3.56	26271	DL-VALINE-2,3,4,4,5,5-D8
Histidine	6.70	27570	GLYCINE-2,2-D2
Glycine	4.64	15428	GLYCINE-2,2-D2
Aspartate	4.16	22660	L-ASPARTIC ACID (13C4, 97-99%; D3, 97-99%; 15N, 97-99%)
Threonine	4.29	26986	L-GLUTAMIC ACID (1,2-13C2)
Glutamic acid	4.20	18237	L-GLUTAMIC ACID (1,2-13C2)

Alanine	4.33	16449	L-ALANINE-d3
Tyrosine	3.56	18186	DL-VALINE-2,3,4,4,5,5-D8
serine	4.87	17822	GLYCINE-2,2-D2
methionine	3.04	16811	DL-LEUCINE-2,3,3-D3
phenylalanine	2.78	28044	Phenylalanine-d5
Kynurenine	2.77	28683	Phenylalanine-d5
4-hydroxyproline	4.19	20392	DL-VALINE-2,3,4,4,5,5-D8
Glycylglycine	4.57	17201	GLYCINE-2,2-D2
Creatinine	1.80	16737	Creatinine-Nmethyl-D3
Glucose	3.76	17234	D-GLUCOSE-13C6, 99% 13C
Sorbitol	3.56	30911	D-GLUCOSE-13C6, 99% 13C
Glucose-6-P	5.66	14314	D-GLUCOSE-13C6, 99% 13C
Fructose-6-P	4.86	88003	D-GLUCOSE-13C6, 99% 13C
Glucose-1-P	4.84	29042	D-GLUCOSE-13C6, 99% 13C
Ribose-5-P	4.67	78679	D-GLUCOSE-13C6, 99% 13C
Ribulose-5-P	4.24	37455	D-GLUCOSE-13C6, 99% 13C
Fructose-1,6-P2	7.90	78682	D-GLUCOSE-13C6, 99% 13C
Lactate	2.56	42111	13C3-lactate
Pyruvate	1.74	32816	13C3-Pyruvate
α-Ketoglutarate	3.56	30915	SUCCINIC ACID (D4)
2-Hydroxybutyric acid	1.86	1148	13C3-Pyruvate
Malic acid	3.82	25115	AMP-13C10,15N5
Succinic acid	2.84	15741	SUCCINIC ACID (D4)
Fumaric acid	4.06	18012	SUCCINIC ACID (D4)
Ascorbic acid	3.56	22651	AMP-13C10,15N5
cis-Aconitate	3.60	32805	ATP-13C10
Glyceraldehyde-3-P	7.20	17138	UTP-13C9,15N2
Dihydroxyacetone phosphate	4.09	16108	L-ALANINE-d3
glutaric acid	3.51	17859	SUCCINIC ACID (D4)
2-aminoadipic acid	3.46	37024	L-GLUTAMIC ACID (1,2-13C2)
phosphoenolpyruvate	4.88	18021	UTP-13C9,15N2
6-phosphogluconic acid	6.38	48928	ATP-13C10
Acetyl-CoA	4.25	15351	L-GLUTAMIC ACID (1,2-13C2)
AMP	3.89	16027	AMP-13C10,15N5
ADP	5.08	16761	ATP-13C10
ATP	6.55	15422	ATP-13C10
IMP	4.16	17202	AMP-13C10,15N5
GMP	4.78	17345	AMP-13C10,15N5
GDP	6.64	17552	UTP-13C9,15N2
GTP	8.69	15996	ATP-13C10
CTP	7.82	17677	UTP-13C9,15N2
UDP	5.53	17659	UTP-13C9,15N2
UTP	7.12	15713	UTP-13C9,15N2
cAMP	2.84	17489	13C3-lactate
NAD+	4.55	15846	AMP-13C10,15N5
NADH	3.85	16908	AMP-13C10,15N5
NADP+	6.00	18009	UTP-13C9,15N2
NADPH	5.49	16474	UTP-13C9,15N2
Xanthine	1.99	15318	Hypoxanthine-2,8,9-D3
Guanosine	3.00	16750	Hypoxanthine-2,8,9-D3
Adenine	1.32	16708	Creatinine-Nmethyl-D3
Uracil	1.06	17568	Hypoxanthine-2,8,9-D3
Hypoxanthine	1.94	17368	Hypoxanthine-2,8,9-D3
Inosine	2.66	17596	Hypoxanthine-2,8,9-D3
Adenosine	4.23	16335	AMP-13C10,15N5
Uridine	2.13	16704	Hypoxanthine-2,8,9-D3
Glutathione	3.92	16856	L-GLUTAMIC ACID (1,2-13C2)
Oxiglutathione	6.27	167606	ATP-13C10

Table S3. Detected acylcarnitines with ChEBI identifier, retention time and corresponding internal standards

Component Name	Retention Time (min)	ChEBI ID	Internal standard
Acetylcarnitine	0.29	73024	Acetylcarnitine-d3
Butyrylcarnitine	1.22	7676	Butyrylcarnitine-d3
Carnitine	0.39	17126	Carnitine-d3
Choline	0.28	15354	Choline-d3
Deoxycarnitine	0.34	16244	Deoxycarnitine-d3
Linoleylcarnitine	7.77	73072	Octadecanoylcarnitine-d3
Malonylcarnitine	0.30	73028	Acetylcarnitine-d3
Methylmalonylcarnitine	0.31	73031	Butyrylcarnitine-d3
Oleoylcarnitine	8.25	72689	Octadecanoylcarnitine-d3
Propionylcarnitine	0.52	28867	Acetylcarnitine-d3
Tiglylcarnitine	1.75	71179	Butyrylcarnitine-d3
Isovalerylcarnitine	2.05	73025	Butyrylcarnitine-d3
2-Methylbutyrylcarnitine	1.98	73026	Butyrylcarnitine-d3

Table S4. Detected signaling lipids with ChEBI identifier, retention time and corresponding internal standards

Metabolite	Retention time (min)	ChEBI ID	Internal standard
ASL_FA18.0	14.08	28842	BSL_d17_FA18.1_w9_ISTD
BSL_FA18.1_w9	13.81	16196	BSL_d17_FA18.1_w9_ISTD
BSL_FA18.2_w6	13.48	17351	BSL_d4_FA18.2_w6_ISTD_2
BSL_FA18.3_w3	13.17	27432	BSL_d5_FA22.6_w3_ISTD
BSL_FA20.4_w6	13.42	15843	BSL_d8_FA20.4_w6_ISTD
BSL_FA20.5_w3	13.13	28364	BSL_d5_FA22.6_w3_ISTD
BSL_FA22.4_w6	13.73	53487	BSL_d17_FA18.1_w9_ISTD
BSL_FA22.5_w3	13.48	61204	BSL_d5_FA22.6_w3_ISTD
BSL_FA22.6_w3	13.35	28125	BSL_d5_FA22.6_w3_ISTD
BSL_FA18.3_w6	13.21	28661	BSL_d5_FA22.6_w3_ISTD
BSL_FA20.3_w6	13.6	53486	BSL_d4_FA18.2_w6_ISTD_2
BSL_FA20.3_w9	13.68	72865	BSL_d17_FA18.1_w9_ISTD
BSL_FA22.5_w6	13.58	61204	BSL_d4_FA18.2_w6_ISTD_2
BSL_a_LEA	11.57	89605	BSL_d4_LEA_ISTD
BSL_POEA	12.06	71465	BSL_d4_OEA_ISTD
BSL_LEA	12.73	64032	BSL_d4_LEA_ISTD
BSL_PEA	13.12	71464	BSL_d4_PEA_ISTD
BSL_1_OG_2_OG	13.55	30916	BSL_d4_OEA_ISTD
BSL_SEA	13.67	85299	BSL_d3_SEA_ISTD
BSL_OEA	13.27	71466	BSL_d4_OEA_ISTD
BSL_9_12_13_TriHOME	3.68	34506	BSL_d4_PGF2a_ISTD
BSL_9_10_13_TriHOME	3.87	34499	BSL_d4_PGF2a_ISTD
BSL_14_15_DiHETE	8.72	88459	BSL_d11_14_15-DiHETrE_ISTD
BSL_12_13_DiHOME	8.95	72665	BSL_d4_12_13_DiHOME_ISTD
BSL_14_15_DiHETrE	9.5	63966	BSL_d11_14_15-DiHETrE_ISTD
BSL_11_12_DiHETrE	9.8	63969	BSL_d11_14_15-DiHETrE_ISTD
BSL_9_HOTrE	9.97	72625	BSL_d4_9_HODE_ISTD
BSL_20_HETE	10.35	34306	BSL_d6_20_HETE_ISTD
BSL_12_HEPE	10.48	72645	BSL_d8_12_HETE_ISTD
BSL_9_HEPE	10.56	89570	BSL_d8_12_HETE_ISTD
BSL_13_HODE	10.7	72639	BSL_d4_9_HODE_ISTD
BSL_12_13_EpOME	11.95	38229	BSL_d4_12_13_DiHOME_ISTD
BSL_5_HEPE	10.73	72627	BSL_d4_9_HODE_ISTD
BSL_9_HODE	10.78	72651	BSL_d4_9_HODE_ISTD
BSL_9_10_EpOME	12.32	34494	BSL_d4_9_10_DiHOME_ISTD
BSL_16_HDoHE	11.08	72613	BSL_d8_12_HETE_ISTD
BSL_8_HDoHE	11.72	72610	BSL_d8_12_HETE_ISTD
BSL_5_HETrE	12.89	88359	BSL_d8_5_HETE_ISTD

Table S5. Metabolites found with regulation after NAD+ treatment

5.1 Comparison of control_Rotenone_NAD versus control_Rotenone group			
Metabolite	**Log2_FoldChange**	**-Log10 (p value with Bonferroni correction)**	**Relative regulation**
GABA	0.30	1.96	UP
Proline	0.23	4.33	UP
Glycine	-0.26	2.72	DOWN
Aspartate	0.15	1.83	UP
Glutamate	0.30	3.13	UP
4-Hydroxyproline	-0.11	1.43	DOWN
Glycylglycine	-0.16	1.46	DOWN
Glucose	1.30	3.30	UP
Sorbitol	-0.30	3.55	DOWN
Fructose-1,6-P2	-0.42	2.10	DOWN
Lactate	-0.92	4.57	DOWN
2-Hydroxybutyric.acid	-0.52	1.47	DOWN
Ascorbic.acid	3.49	3.30	UP
AMP	-0.87	3.13	DOWN
ADP	-0.40	1.67	DOWN
IMP	1.25	1.50	UP
GMP	-0.85	3.62	DOWN
GDP	-0.44	3.18	DOWN
CTP	0.26	1.57	UP
cAMP	2.57	2.70	UP
Xanthine	-0.36	1.65	DOWN
Guanosine	-0.71	1.41	DOWN
Hypoxanthine	0.82	4.53	UP
Inosine	1.07	1.78	UP
Uridine	-0.44	1.99	DOWN
cis-Aconitate	1.60	3.30	UP
Glyceraldehyde-3-P	-0.49	1.67	DOWN
Glutaric.acid	-0.87	4.97	DOWN
UDP	-0.47	1.67	DOWN
NAD+	2.32	3.66	UP
Acetylcarnitine	-0.28	1.49	DOWN
Butyrylcarnitine	-0.75	4.05	DOWN
Choline	-0.24	1.75	DOWN
Malonylcarnitine	-1.66	5.12	DOWN
Oleoylcarnitine	-1.29	3.07	DOWN
Propionylcarnitine	1.29	3.51	UP
Tiglylcarnitine	0.81	4.25	UP
Isovalerylcarnitine	1.62	5.12	UP
2-Methylbutyroylcarnitine	2.00	6.50	UP
Deoxycarnitine	-0.67	2.12	DOWN
Linoleylcarnitine	-1.20	3.15	DOWN
FA20.4_n6	0.37	1.67	UP
FA20.5_n3	0.20	1.45	UP
FA22.5_n3	0.57	3.61	UP

FA22.6_n3	0.41	2.20	UP
FA18.3_n6	-0.38	2.63	DOWN
9,12,13-TriHOME	-0.60	3.73	DOWN
9,10,13-TriHOME	-0.49	3.73	DOWN
14,15-DiHETE	0.70	3.83	UP
14,15-DiHETrE	1.06	6.50	UP
20-HETE	-0.28	1.97	DOWN
13-HODE	-0.64	3.93	DOWN
16-HDoHE	0.37	3.37	UP

5.2 Comparison of PINK1_Rotenone_NAD versus PINK1_Rotenone group

Metabolite	Log2_FoldChange	-Log10 (p value with Bonferroni correction)	Relative regulation
Leucine	-0.25	1.71	DOWN
Betaine	-0.30	2.61	DOWN
Valine	-0.31	2.61	DOWN
Tyrosine	-0.23	2.07	DOWN
Sorbitol	-0.49	4.43	DOWN
Lactate	-0.55	3.54	DOWN
Ascorbic.acid	2.60	4.86	UP
AMP	-0.58	1.64	DOWN
IMP	0.60	1.32	UP
Adenosine	-0.88	2.51	DOWN
cis-Aconitate	1.45	2.51	UP
NAD+	2.09	2.61	UP
NADP+	0.32	1.32	UP
Malonylcarnitine	-0.93	3.22	DOWN
Propionylcarnitine	1.33	3.10	UP
Tiglylcarnitine	1.10	2.98	UP
Isovalerylcarnitine	2.01	1.50	UP
2-Methylbutyroylcarnitine	3.10	1.34	UP
FA18.1_n9	-0.25	2.81	DOWN
FA20.4_n6	0.37	2.76	UP
FA20.3_n9	0.22	1.77	UP
FA20.3_n6	0.22	1.32	UP
FA22.5_n6	0.48	3.24	UP
9,12,13-TriHOME	-0.80	4.84	DOWN
9,10,13-TriHOME	-0.75	4.61	DOWN
14,15-DiHETE	0.42	3.18	UP
14,15-DiHETrE	0.70	5.70	UP
13-HODE	-0.45	2.08	DOWN
12-HEPE	-0.43	2.08	DOWN

5.3 Comparison of PINK1_NAD versus PINK1 group			
Metabolite	**Log2_FoldChange**	**-Log10 (p value with Bonferroni correction)**	**Relative regulation**
Hypoxanthine	1.06	1.82	UP

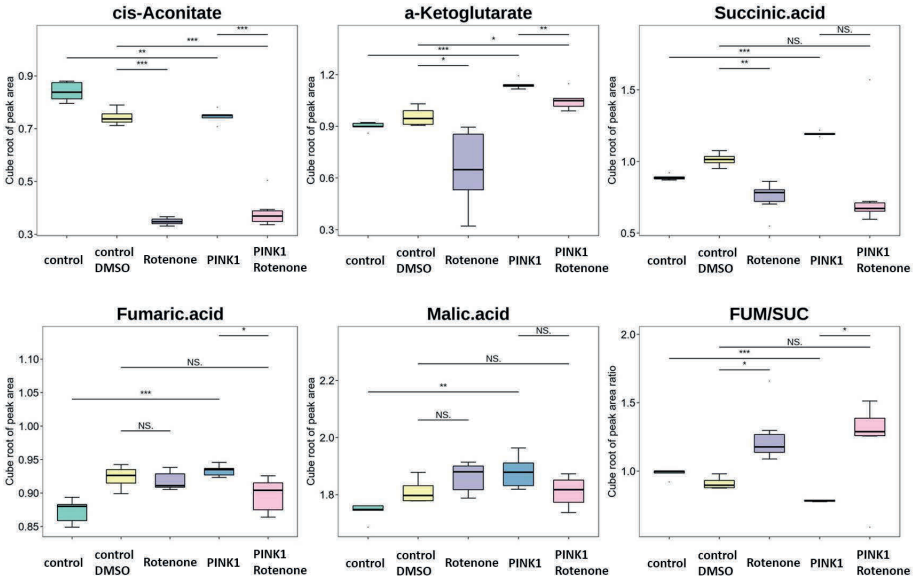

Figure S1. Metabolite changes representing TCA cycle metabolism changes in control and PINK1 mutated neuron influenced by rotenone. Box plot for showing the levels of TCA cycle intermediates in control groups (control and control_DMSO), rotenone-treated control group (Rotenone), PINK1-mutated group (PINK1) and rotenone-treated PINK1-mutated group (PINK1_Rotenone). Significant difference between group comparison was marked by * ($p < 0.05$), ** ($p < 0.01$), *** ($p < 0.001$). No significant difference was marked by NS.

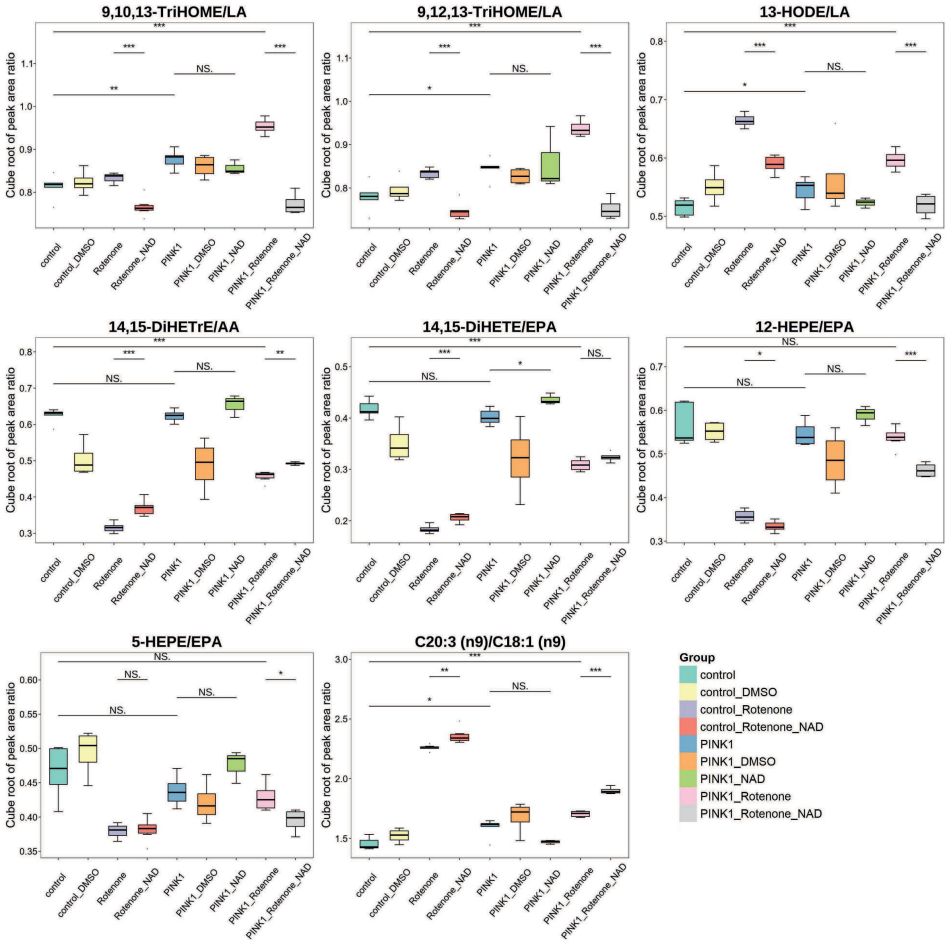

Figure S2. Box plot for showing NAD+ treatment regulation on the metabolite ratio level of poly unsaturated fatty acid oxidation for rotenone-treated control group (Rotenone), PINK1-mutated group (PINK1) and rotenone-treated PINK1-mutated group (PINK1_rotenone). Significant difference between group comparison was marked by * ($p < 0.05$), ** ($p < 0.01$), *** ($p < 0.001$). No significant difference was marked by NS.